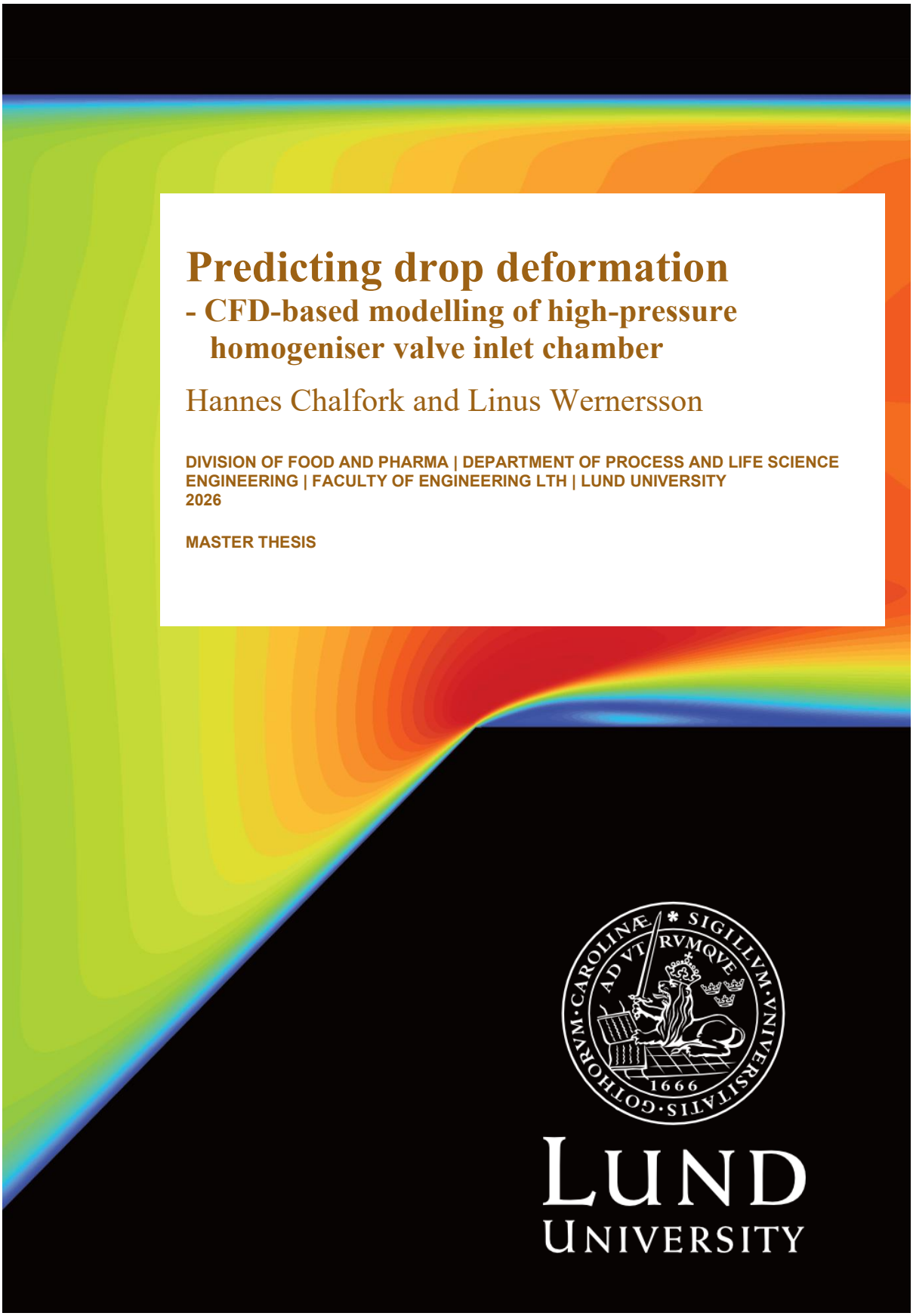

Predicting drop deformation

- CFD-based modelling of high-pressure homogeniser valve inlet chamber

Hannes Chalfork and Linus Wernersson

DIVISION OF FOOD AND PHARMA | DEPARTMENT OF PROCESS AND LIFE SCIENCE ENGINEERING | FACULTY OF ENGINEERING LTH | LUND UNIVERSITY

2026

MASTER THESIS

LUND UNIVERSITY

Predicting drop deformation

CFD-based modelling of high-pressure homogeniser valve inlet chamber

Hannes Chalfork and Linus Wernersson

LUND
UNIVERSITY

Predicting drop deformation

CFD-based modelling of high-pressure homogeniser valve inlet chamber

Published by
Department of Process and Life Science Engineering
Faculty of Engineering LTH, Lund University
P.O. Box 118, SE-221 00 Lund, Sweden

Subject: KLTM06 Degree Project in Food Engineering, Nutrition and Food Chemistry
Division: Division of Food and Pharma
Supervisor: Andreas Håkansson
Examiner: Anna Fureby

Predicting drop deformation

CFD-based modelling of
high-pressure homogeniser valve inlet chamber

by

Hannes Chalfork & Linus Wernersson

Process and Life Science Engineering – Division of Food and Pharma

June 2026

Supervisor: Andreas Håkansson
Examiner: Anna Fureby

Simulering av fettdroppar i mjölk

I arbetet mot en mer hållbar livsmedelsproduktion är energiförbrukning en viktig fråga, inte minst inom mejeriindustrin. Mejeriindustrin kräver flera steg från råmjölk till färdig produkt och för att kunna minska energiförbrukningen i mejerier behöver vi undersöka hur dessa processer kan optimeras. Idealt bör detta undersökas experimentellt, men fysiska experiment är tidskrävande och kan behöva dyr utrustning. Genom att matematiskt simulera processerna kan man med hjälp av bara datorn undersöka hur mjölkproduktionen kan göras mer effektiv. I detta fall genom att studera deformationsbeteende av fettdroppar i vätskeflöden.

Mjölk, komjölk såväl som växtbaserade alternativ, är emulsioner bestående av små fettdroppar i vattenlösning. Alla emulsioner kommer, för eller senare, att skikta sig då den feta fasen sammansluter och skiljer sig från vattenfasen. Hur lång tid denna process tar varierar, men ju mindre fettdropparna är desto längre tid tar det. Homogenisering är en mejeriteknisk process för att minska fettdropparnas storlek. Detta görs i en homogenisator där råmjölken pumpas in genom en ventil med en väldigt smal spalt, ungefär lika brett som ett hårstrå, under högt tryck. Detta görs att fettdropparna slås sönder och finfördelas vilket ger en homogeniserad mjölk som inte skär sig, eller snarare skär sig långt efter att den surnat och blivit oduglig av andra skäl. I princip all mjölk du köper i affären är homogeniserad.

Tidigare forskning har visat att fettdropparna går sönder strax efter spaltens utlopp. Däremot deformeras dropparna redan innan de kommet fram till spalten, i vad som kallas inloppskammaren. Den här processen har dock mycket låg effektivitet, bara 0.01% av energin som används går åt att slå sönder dropparna. Eftersom effektiviteten är så låg kan en liten ökning av effektiviteten ge stor påverkan i minskad energiförbrukning. Genom att förstå hur fettdropparna deformeras i inloppskammaren och vilka metoder som kan användas för att förutse deformationsbeteendet, kan ventilen i homogenisatorn lättare konstrueras på ett sätt som minskar dess energibehov.

I det här examensarbetet undersöker vi hur fettdroppar beter sig i inloppskammaren och hur man kan modellera dem på ett enkelt sätt. Först undersöks hur droppar beter sig i en platt modell i labbskala med hjälp av en höghastighetskamera. Dropparna detekteras i varje bild och deformationen mäts. Därefter utförs två sorters simuleringar som mäter deformationen med numerisk strömningsmekanik vilket är sätt att matematiskt beräkna hur vätskor rör sig.

Resultaten visar att båda dessa simuleringar kan förutsäga hur dropparna i den experimentella uppsättningen deformeras på ett sätt som inte kräver mycket beräkningskraft. Det innebär att det i framtiden kanske inte krävs experimentell utrustning för att utforma effektivare homogenisatorventiler. Vilket kan underlätta framtida utveckling av homogenisatorer med minskad energiförbrukning.

Abstract

High-pressure homogenisers (HPHs) are used for a variety of food products to create emulsions. It is interesting both from a sustainable and economical perspective to make HPHs more energy efficient due to their high energy demand and low efficiency. Previous research has shown that drop deformation is affected by the whole HPH valve geometry, including the inlet chamber, and it is hypothesised that droplets can be primed for breakup.

This project aims to evaluate how well two computational fluid dynamics (CFD) methods predict viscous drop deformation in the inlet chamber of a lab-scale HPH valve model. The first method involves using mathematical models based on velocity gradient data from 1D discrete phase method (DPM) CFD simulations. The second method includes a 2D Volume of Fluid (VoF) CFD simulation where the spatial resolution of the droplets is considered. Both methods were compared to experimental observations with respect to degree of deformation, location of deformation and to the dimensionless Capillary number.

Drop release events were recorded with a high-speed camera on an experimental HPH valve model with a gap height of 0.75 mm for three different volumetric flow rates. The recordings show that the droplets start deforming at two gap lengths before the gap inlet and reach their maximum deformation within one gap length after the gap inlet. Lower volumetric flow rates give larger droplets and more deformation. A trend of increasing deformation with increasing Capillary number is shown for all three data series. However, each data set is separated from each other in the degree of formation at similar Capillary numbers. This suggests that the Capillary number does not capture the drop deformation on its own in this HPH valve setup.

For the 1D DPM method, two out of the three mathematical models predict the deformation well with regards to the degree of deformation. However, the position of the deformation maxima differed slightly from the experimental maxima for both models. This can be explained by the 1D method considering the droplets as point objects, in contrast to the 2D VoF method which account for spatial resolution and predicts the location of the deformation maxima well. However, the 2D VoF simulations require an effective interfacial tension 16 times higher than the real interfacial tension to yield similar degrees of deformation as the empirical data. Similar to the empirical data, the 2D VoF simulations show increasing degree of deformation with increasing Capillary number. However, the 2D VoF method does not reproduce a clear separation in deformation magnitude between volumetric flow rates as experimentally observed.

These results show that both CFD methods predict drop deformation well. The 1D DPM method is advantageous since it requires significantly less computational power.

Sammanfattning

Högtryckshomogenisatorer (HPH) används för en mängd olika livsmedelsprodukter för att skapa emulsioner. Det är intressant både ur hållbarhets och ekonomiska perspektiv att göra HPH mer energieffektiva på grund av deras höga energiförbrukning och låga effektivitet. Tidigare forskning har visat att droppdeformation påverkas av hela HPH-ventilens geometri, inklusive inloppskammaren, och det antas att droppar kan förberedas för att slås sönder.

Detta projekt ämnar att utvärdera hur väl olika prediktionsmodeller baserade på numerisk strömningsmekanik (CFD) förutsäger viskös droppdeformation i inloppskammaren för en experimentell modell av en HPH-ventil i laboratorieskala. Den första metoden går ut på att kombinera matematiska deformationsmodeller med hastighetsgradientdata från steady-state 1D CFD-simuleringar med diskretfasmetod (DPM). Den andra metoden bygger på transient 2D Volume of Fluid (VoF) CFD-simulering där dropparnas upplösning i tid och rymd beaktas. Båda metoderna jämfördes med empiriska observationer med avseende på deformationsgrad, deformationens placering i flödeskammaren och det dimensionslösa kapillärtalet.

Vattenflöden med fettdroppar undersöktes med en höghastighetskamera, monterad på en experimentell HPH-ventilmodell med spalthöjden 0,75 mm, för tre olika volymetriska flödeshastigheter. Bildserierna visar att dropparna börjar deformeras vid två spaltlängder före spaltinloppet och når sin maximala deformation inom en spaltlängd efter spaltinloppet. Lägre volymetriska flödeshastigheter ger större droppar med mer deformation. Alla volymetriska flödeshastigheter visade en trend av ökande deformation med ökande kapillärtal. Däremot skiljer sig alla dataserier från varandra i deformationsgrad vid liknande kapillärtal. Detta tyder på att kapillärtalet inte fångar hela droppdeformationsbeteendet på egen hand i denna experimentella uppsättning.

Två av de tre matematiska modellerna för droppdeformation med 1D DPM-metoden modellera deformationen väl, med avseende på deformationsgraden. Positionen för deformationsmaxima skilde sig däremot lätt från det empiriska maximat för båda modellerna. Detta kan förklaras genom att 1D-metoden betraktar dropparna som punktobjekt, i motsats till 2D VoF-metoden som tar hänsyn till rymdupplösningen och förutsäger deformationsmaximans plats väl. 2D VoF-simuleringarna kräver dock en effektiv ytspänning som är 16 gånger högre än den verkliga ytspänningen för att ge liknande grader av deformation som den empiriska datan. I likhet med den empiriska datan visar 2D VoF-simuleringarna ökande grad av deformation med ökande kapillärtal. 2D VoF-metoden reproducerar dock inte en tydlig skillnad i deformationsstorlek mellan volymetriska flödeshastigheter som experimentellt observerats.

Resultaten visar att båda CFD-metoderna förutsäger droppdeformation väl. 1D DPM-metoden är fördelaktig eftersom den kräver betydligt mindre beräkningskraft.

Acknowledgement

We would like to express our gratitude to Prof. Andreas Håkansson who has been a most excellent supervisor, always responsive and eager to provide guidance and answer questions. You have gone above and beyond with providing a custom crash-course in CFD, literature recommendations and valuable insights. Your enthusiastic support has made this project an educative and rewarding experience.

We also want to show our appreciation towards our fellow master students at the department from whom we have received support throughout the writing process. A lot of laughter has been shared with you, both inside the thesis office and during the fika breaks. Special thanks to Witko Tamm for sharing helpful insights in all matters Python and IT-related, and for being an invaluable discussion partner in our shared CFD struggles.

Thank you!
Hannes Chalfork, Linus Wernersson

Table Of Contents

Abbreviations and nomenclature

Abbreviations

Abbreviation	Full Name
CFD	Computational Fluid Dynamics.
DPM	Discrete Phase Method.
HPH	High-Pressure Homogeniser.
LOWESS	Locally Weighted Scatterplot Smoothing.
MM	Mafettone-Minale.
RANS	Reynolds Averaged Navier Stokes.
RNG	Renormalisation Group.
std	Standard deviation.
VoF	Volume of Fluid.

Greek Symbols

Letter	Description	Unit
α	Flow type.	none
β_n	Eigenmode dampening rate.	s^{-1}
${\beta_n}^0$	Inviscid eigenmode dampening rate.	s^{-1}
γ	Interfacial tension coefficient.	$N \cdot m^{-1}$
γ_{eff}	Effective interfacial tension coefficient.	$N \cdot m^{-1}$
$\dot{\gamma}$	Shear rate.	s^{-1}
Δl	Control space length.	m
$\Delta Pa_{LaPlace}$	LaPlace pressure.	Pa
Δt	Time step length.	s
$\dot{\varepsilon}$	Elongation rate.	s^{-1}

θ	Angle between major elliptical axis and fluid flow direction.	$^\circ$
Λ_α	Inlet chamber angle of slope.	$^\circ$
λ	Viscosity ratio μ_D/μ_C.	none
$\hat{\mu}$	Inverse viscosity ratio μ_C/μ_D.	none
μ_C	Dynamic viscosity of the continuous phase.	$\mathrm{Pa \cdot s}$
μ_D	Dynamic viscosity of the dispersed phase.	$\mathrm{Pa \cdot s}$
$\hat{\rho}$	Density fraction of continuous and dispersed phases ρ_C/ρ_D.	none
ρ_C	Density of the continuous phase.	$\mathrm{kg \cdot m^{-3}}$
ρ_D	Density of the dispersed phase.	$\mathrm{kg \cdot m^{-3}}$
σ_{eff}	Effective deformative stress.	Pa
σ_{def}	Deformative stress.	Pa
σ_{stab}	Stabilizing stress.	Pa
τ	Time scale.	s
ω_n	Eigenmode angular frequency.	$\mathrm{rad \cdot s^{-1}}$
${\omega_n}^0$	Inviscid frequency.	$\mathrm{rad \cdot s^{-1}}$

Latin Symbols

Letter	Description	Unit
A	Oscillation amplitude.	m
$A_{ellipse}$	Area of ellipse.	m^2
B	Droplet minor axis length.	m
Ca	Capillary number.	none
$\overline{Ca}$	Average capillary number of population.	none
Ca_{crit}	Critical capillary number.	none
Co	Courant number.	none
D_0	Initial droplet diameter.	m
$\overline{D_0}$	Average initial droplet diameter of population.	m
$\boldsymbol{E}$	Deformation rate tensor.	s^{-1}
$\widehat{\boldsymbol{E}}$	Deformation rate tensor, dimensionless.	none
f_1, f_2	Viscosity dependent coefficients.	none
G	Velocity gradient.	s^{-1}
h	Height of flow cell gap inlet.	m
$\boldsymbol{III}_{\widehat{\boldsymbol{S}}}$	Determinant of $\widehat{\boldsymbol{S}}$.	m^4
$\boldsymbol{II}_{\widehat{\boldsymbol{S}}}$	Second invariant of $\widehat{\boldsymbol{S}}$.	m^6
$\boldsymbol{I}$	Second rank unit tensor.	none
K	Dimensionless constant in the Lamb equation.	none
L	Major elliptical axis.	m
L_q	Gap length.	m
$\left(\overline{L/B}\right)_{max}$	Average elongational deformation maxima of population.	none
Q	Volumetric flowrate.	$m^3 \cdot s^{-1}$
Re_{osc}	Oscillatory Reynolds number.	none

r_1, r_2	Principal radii of curvature.	m
$\boldsymbol{S}$	Droplet shape tensor.	m^2
$\widehat{\boldsymbol{S}}$	Droplet shape tensor, dimensionless.	none
T_n	Miller-Scriven time factor	s^{-1}
Tr	Trouton number.	none
T_y	Taylor's viscosity factor	None
$\hat{t}$	Dimensionless Maffetone-Minale/Lamb time.	none
U_g	Average gap inlet fluid velocity.	$\mathrm{m} \cdot \mathrm{s}^{-1}$
$\boldsymbol{V}$	Velocity gradient tensor.	$\mathrm{m} \cdot \mathrm{s}^{-1}$
v	Fluid flow speed.	$\mathrm{m} \cdot \mathrm{s}^{-1}$
v_{in}	Fluid flow speed, at flow cell inlet.	$\mathrm{m} \cdot \mathrm{s}^{-1}$
v_{out}	Fluid flow speed, at flow cell outlet.	$\mathrm{m} \cdot \mathrm{s}^{-1}$
$\boldsymbol{W}$	Vorticity tensor.	$\mathrm{m} \cdot \mathrm{s}^{-1}$
$\widehat{\boldsymbol{W}}$	Vorticity tensor, dimensionless.	none
We	Weber number.	none
We_d	Weber model empirical constant.	none
$We_{d,opt}$	Weber model empirical constant, optimised.	none
X	Dimensionless dampening rate.	none
x	Flow cell geometry horizontal length.	m
x_g	Horizontal position of gap inlet, in the flow cell geometry.	m

1 Introduction

Liquid-liquid emulsions make up a wide variety of food products, for instance dairy emulsions, sauces and salad dressings where High-Pressure Homogenisers (HPHs) are widely used (Kadian et al., 2021; Roobab et al., 2023; Schultz et al., 2004). The homogenisation process is energy demanding with a low energy efficiency, resulting in high operational costs (Håkansson, 2022). However, HPHs are still one of the most efficient technologies to create emulsions in continuous industrial production (Stang et al., 2001). Decreasing the energy demand is therefore interesting from both a sustainable and economical perspective.

A HPH valve inlet chamber and gap is illustrated in Figure 1 where fluid enters axially (here, in the y-direction outside of the illustration) through a feed pipe by a high-pressure piston pump and is forced radially towards a narrow gap between the forcer and the seat (Håkansson, 2015; Innings, 2015). Before the gap, the seat is often inclined which creates the narrowing inlet chamber. The fluid exits the gap to the outlet chamber which has a larger volume. Previous research has shown that drop breakup occur in the outlet chamber and many agree that this is because of interactions with turbulent jets (Innings & Trägårdh, 2005; Kelemen et al., 2015; Mutsch et al., 2021). However, recent studies has revealed that droplets also can break within the gap, although at a significantly lower rate (Håkansson, 2025).

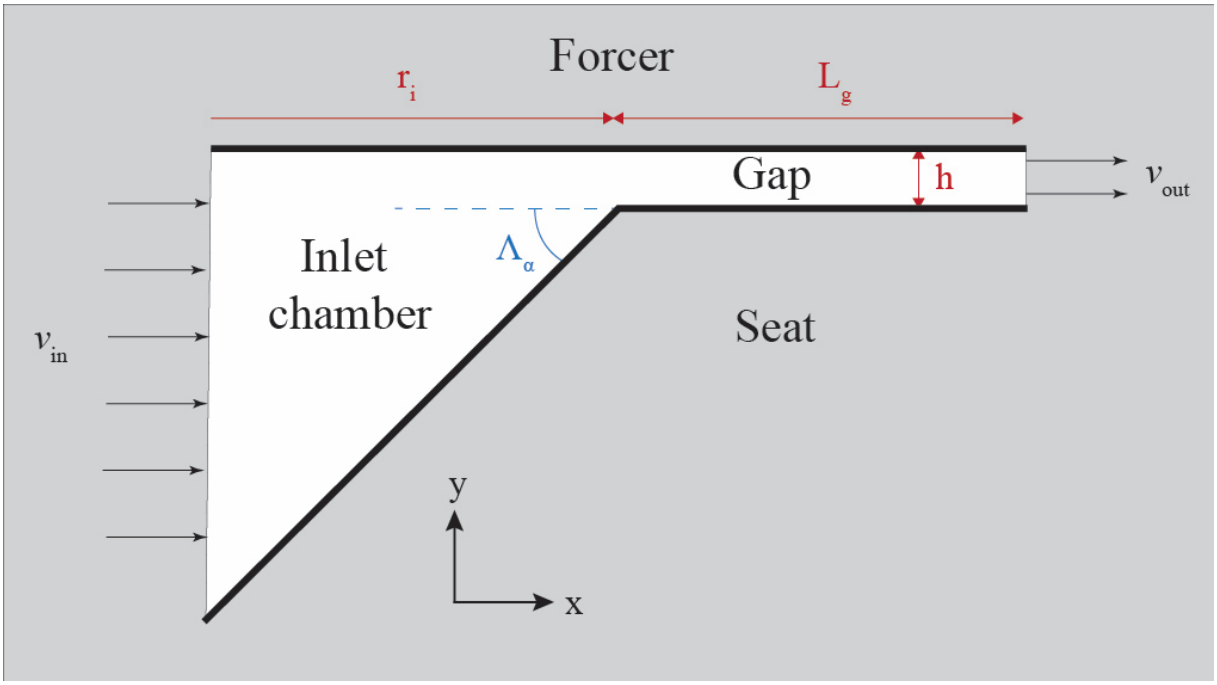

Figure 1: illustration of the inlet chamber and gap of a lab-scale HPH valve with velocity in, v_{in} and out, v_{out}, gap inlet radius r_i measured from the axial centre, gap length L_g, gap height, h, and gap inlet angle, Λ_α.

These findings suggest that the focus on HPH optimisation should be to control the turbulence in the outlet chamber. This can be affected by the whole valve geometry, including the inlet chamber where the droplets could be primed for breakup before the gap (Håkansson, 2022, 2025). Understanding drop deformation behaviour in the inlet chamber can be done experimentally by changing the dimensions and inlet chamber angle Λ_α. However, if drop deformation can accurately be predicted by simulations, it would facilitate easier design optimisation without the need of physical models.

One approach is to use simple 1D steady-state Discrete Phase Model (DPM) Computational Fluid Dynamics (CFD). Combined with simple mathematical deformation models this can predict drop deformation behaviour. In this application, 1D DPM CFD involves using a 2D simulation where DPM data is extracted as 1D trajectories. An alternative approach is to simulate drop deformation directly with a multi-phase 2D Volume of Fluid (VoF) CFD simulation, which accounts for the spatial resolution of the droplets in two dimensions.

1.1 Aim

The aim of this thesis is to understand how emulsion droplet properties and device characteristics influence the deformation behaviour in a lab-scale HPH inlet valve and how it can be modelled. This is done by observing previously recorded empirical data from a lab-scale HPH inlet valve setup. Prediction methods include mathematical deformation models based 1D DPM CFD data, and simple 2D VoF CFD simulations. By improving fundamental understanding of droplet deformation in HPH valves this thesis aims to allow further HPH design optimisation.

1.2 Objectives

- Investigate how drop deformation behaviour depends on drop diameter and volumetric flow rate based on previously recorded empirical data of a lab-scale HPH valve setup.

- Investigate how well simple mathematical models can predict drop deformation based on data from 1D steady-state Discrete Phase Model (DPM) CFD simulations.

- Investigate if the observed drop deformation can be accurately reproduced with simple 2D Volume of Fluid (VoF) CFD simulations.

2 Theoretical background

This section first describes fundamental concepts for drop deformation theory and then an explanation of the governing equations for the deformation models used in this thesis. For the following equations, the subscript C, for example ρ_C, denotes the continuous phase (the bulk) and the subscript D, for example ρ_D, denotes the droplet.

2.1 Previous research on droplet deformation

Extensive research has been made on droplet behaviour in fluids. In the 1930s, Taylor extended Einstein's work on solid spheres suspended in fluids and wrote the small deformation theory of droplets in steady-state (Taylor, 1932, 1934). Note that the small deformation theory was derived from observations on stationary droplets in a four-roll mill setup (see Taylor (1934)), whereas this research is focused on continuous flow. Taylor (1934) showed that for a spherical droplet in equilibrium, the Laplace pressure equals the deformation stress from outer forces:

$$\gamma \cdot \left(\frac{1}{r_1} + \frac{1}{r_2}\right) = p_D - p_C + constant, \tag{1}$$

where γ is the interfacial tension constant ($N \cdot m^{-1}$), r_1 and r_2 are the principal radii of the curvature of a droplet (m), p_D and p_C are the inner droplet and outer fluid pressure, respectively ($N \cdot m^{-2}$) (Siqveland & Skjæveland, 2021; Taylor, 1934). This was elaborated to a relationship between the length L and width B of an ellipse to the viscosity ratio $\lambda = \mu_D/\mu_C$ of the droplet viscosity, μ_D (Pa·s) and continuous phase viscosity, μ_C (Pa·s):

$$\frac{L-B}{L+B} = \frac{\mu_C \cdot G \cdot D_0}{\gamma} \cdot \frac{19\lambda + 16}{16\lambda + 16} = \frac{\mu_C \cdot G \cdot D_0}{\gamma} \cdot T_y(\lambda). \tag{2}$$

Here, D_0 is the initial drop diameter (m), T_y is Taylor's viscosity factor which depends on λ, and G describes the velocity gradient (s^{-1}) defined as the sum of the axial velocity gradient (dv_x/dx) and radial velocity gradient (dv_y/dy) of the droplet (Kelemen et al., 2015):

$$G = \left|\frac{dv_x}{dx}\right| + \left|\frac{dv_y}{dy}\right|. \tag{3}$$

The drop deformation has been shown to correlate to several dimensionless numbers where the Weber number (We) has been one of the main ones studied to predict breakup probability and can be defined differently depending on the type of flow (Håkansson, 2025; Ni, 2024; Qi et al., 2022). For this application with laminar flow in the inlet chamber, the We number is defined as (Håkansson, 2022; Risso & Fabre, 1998):

$$We = \frac{\rho_C \cdot G \cdot D_0}{\gamma}, \tag{4}$$

where ρ_C is the continuous phase density (kg·m^{-3}). The We number relates the inertial forces on a drop to the surface tension forces. Over a certain value, droplets typically break and different viscosities give different breakup morphologies (Håkansson et al., 2022). However, in the inlet chamber of this application low inertial forces are assumed. Another dimensionless number called the Capillary number (Ca) relates the viscous forces to the surface tension forces (Hill, 1998; Ni, 2024; Omidvar & Khaleghi, 2012). Since the Ca number instead takes viscous forces into account, it is more suitable for this study. The Ca number is defined as (Stone, 1994):

$$Ca = \frac{\mu_C \cdot G \cdot D_0}{2\gamma}. \tag{5}$$

Similar to the We number, the Ca number also has a critical limit (Ca_{crit}) over which drops break (Bentley & Leal, 1986; Hill, 1998; Kelemen et al., 2015) and the dependence of the Ca number and viscosity ratio shown in Figure 2 has been studied by Hill (1998). However, breakup also requires a critical deformation time (Kelemen et al., 2015; Qi et al., 2022). If a droplet passes through a zone too fast even though the zone provides high enough stress to reach Ca_{crit}, the droplet does not necessarily break and instead returns to its spherical state. In steady-state conditions, droplets would have enough time to reach break while it is not necessarily the case in dynamic flow.

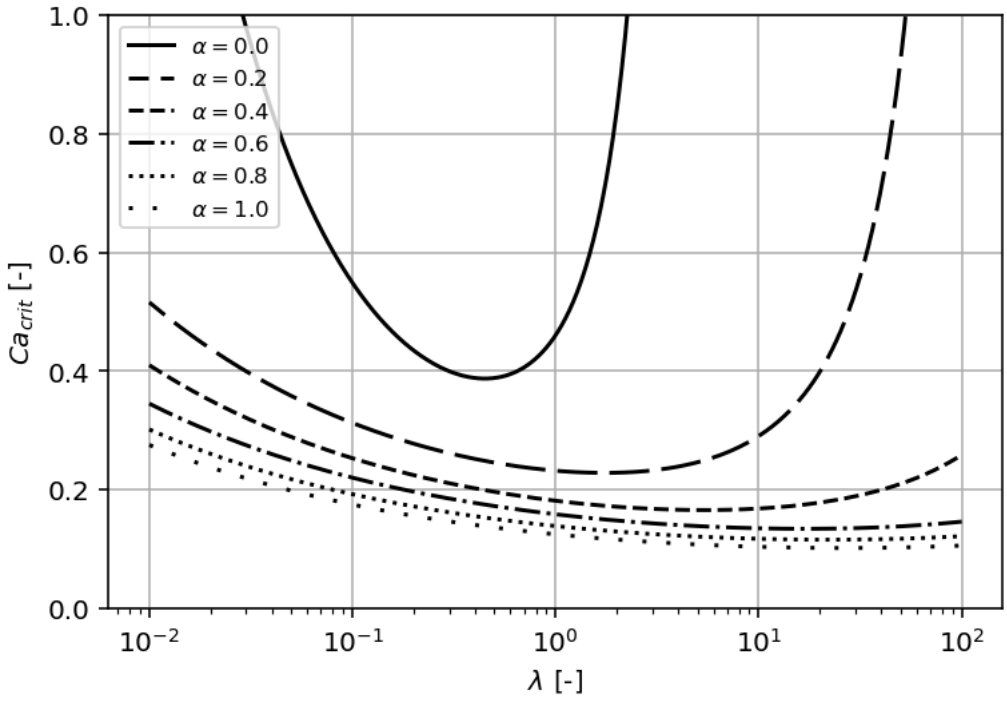

Figure 2: Critical capillary numbers (Ca_{crit}) by viscosity ratio, λ, at different flow types, α, with data from Hill (1998).

The Ca_{crit} depends both on λ and the flow type, α, which relates the elongation rate, $\dot{\varepsilon}$ (s^{-1}) and shear rate, $\dot{\gamma}$ (s^{-1}), of a droplet:

$$\alpha = \frac{\dot{\varepsilon}}{|\dot{\varepsilon}| + |\dot{\gamma}|}, \tag{6}$$

where $-1 \leq \alpha \leq 1$. A flow type of $\alpha = -1$ means equal elongation in all directions, leading to no deformation, $\alpha = 0$ means simple shear flow where the fluid flows as parallel planes and may cause rotation and $\alpha = 1$ means pure shear flow, also called elongation flow, where the flow causes deformation in one direction and elongation in the perpendicular direction and causes no rotation (Bentley & Leal, 1986; Windhab et al., 2005). If the direction of the flow is in the x-axis, it follows that $\dot{\varepsilon} = dv_x/dx$ and $\dot{\gamma} = dv_y/dy$. An illustration of the flow types is shown in Figure 3. Previous research on a modified homogenisation orifice has shown that pure shear flow dominates in most of the inlet chamber while simple shear flow dominates along the inlet chamber walls and within the gap (Kelemen et al., 2015).

This research has provided a foundation for constructing empirical models to describe the deformation behaviour of droplets explained in the following section.

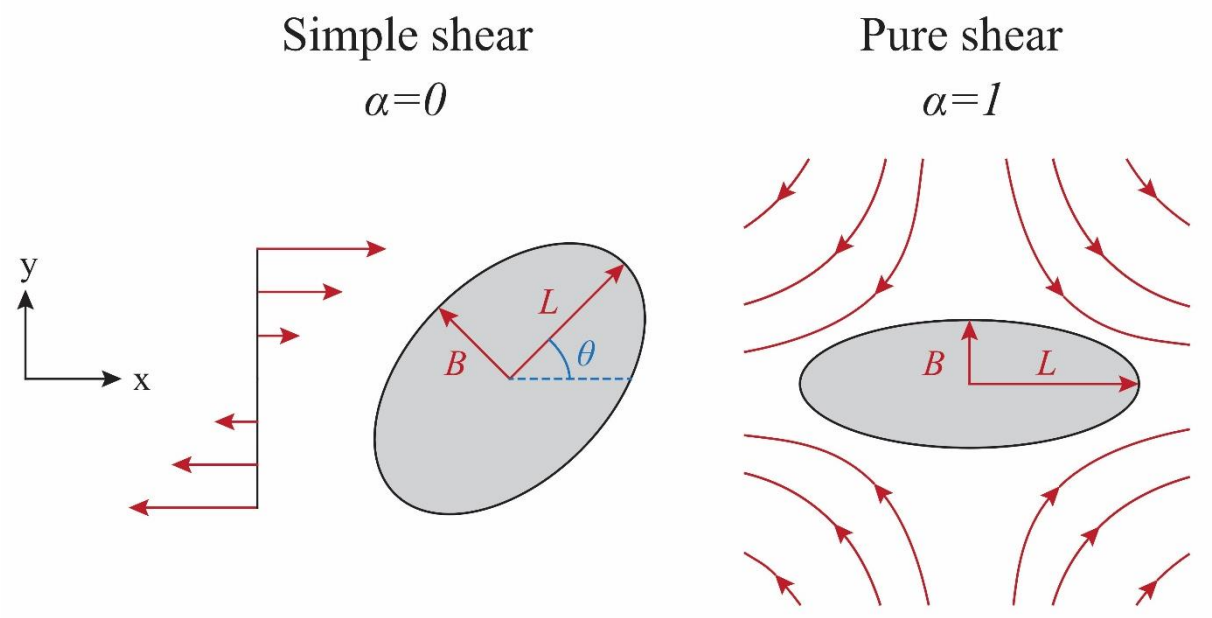

Figure 3: illustration of simple shear and pure shear flow types. Simple shear has a linear velocity gradient from parallel layers of fluid which can cause a rotation of the droplet with the angle θ. Pure shear flow, also called elongational flow, has no rotation where the droplet elongates in one direction, here the flow direction x, and compresses in the perpendicular direction, y.

2.2 Deformation models

In this study, three drop deformation models are used to evaluate the drop deformation based on velocity gradients. The dynamic Weber number (Weber) model, the Maffettone-Minale (MM) model and the Lamb model are described below. For low deformation, the deformation of stationary droplets in steady-state is typically calculated as $(L-B)/(L+B)$, as proposed by Taylor (1934), while L/B is typically used for large deformation (Stone, 1994). For this study, L/B will be used.

2.2.1 The dynamic Weber number model

Innings et al. (2005) suggested a drop simulation method called the dynamic Weber number model for elliptical droplets as an extension to Taylor's small deformation theory. The extension introduces an empirical fitting parameter called the dynamic Weber number (We_d) which considers other dynamic effects, for instance the circulation within the droplet which depends mainly on the λ. This has previously been neglected due to the high viscosity of the droplet (Walstra & Smulders, 1998).

From the Taylor model, the effective stress (σ_{eff}) is defined as the difference between the deformation stress (σ_{def}) and the deformation resistance (σ_{stab}), also called the Laplace pressure:

$$\sigma_{eff} = \sigma_{def} - \sigma_{stab}. \tag{7}$$

The deformation stress on the drop is defined as:

$$\sigma_{def} = Tr \cdot \mu_C \cdot G, \tag{8}$$

where Tr is the dimensionless Trouton number which relates elongation and shear viscosity and is assumed to be 2 for two-dimensional (planar) elongational flow of Newtonian fluids (Walstra & Smulders, 1998, p. 61f). The deformation resistance is defined as:

$$\sigma_{stab} = 2\gamma \cdot \frac{L-B}{L \cdot B}. \tag{9}$$

Eq. 8 and 9 are inserted into Eq. 7 and to consider the other dynamic effects, the We_d is introduced, which yields:

$$\sigma_{eff} = 2\mu_C \cdot G - 2We_d \cdot \gamma \cdot \frac{L-B}{L \cdot B}. \tag{10}$$

The elongation rate from the effective stress is:

$$\frac{du}{dx} = \frac{\sigma_{eff}}{\mu_C} \tag{11}$$

and is used to model the elongation rate numerically with:

$$\frac{dL}{dt} = \frac{du}{dx} \cdot L = 2L \cdot G - 2We_d \cdot \frac{\gamma}{\mu_C} \cdot \frac{L-B}{B}. \tag{12}$$

We_d was determined experimentally by Innings et al. (2005) by analysing the drop at equilibrium where $dL/dt = 0$, resulting in a similar expression as the We number in Eq. 4:

$$We_d = \frac{L \cdot B \cdot G \cdot \mu_C}{\gamma \cdot (L-B)}. \tag{13}$$

We_d depends on the λ and is scaled in a similar way as Taylor's scaling factor in Eq. 2 for small deformations by rearranging Eq. 13 to:

$$\frac{L-B}{L} = \frac{G \cdot B \cdot \mu_C}{\gamma} \cdot \frac{1}{We_d}, \tag{14}$$

and comparing Eq. 2 and Eq. 14, gives the scaling relationship to compare two viscosity ratios:

$$\frac{We_d(\lambda_1)}{We_d(\lambda_2)} = \frac{T_y(\lambda_2)}{T_y(\lambda_1)}. \tag{15}$$

2.2.2 The Maffettone-Minale model

The MM model assumes that droplets are always ellipsoidal (Maffettone & Minale, 1998; Taglienti et al., 2023). This assumption holds until it approaches the Ca_{crit} (Guido & Villone, 1998), and since low Ca numbers are expected for the inlet chamber, the droplets are assumed to be ellipsoidal. The drop shape tensor $\boldsymbol{S}$ of rank two is used to describe the drop shape where the eigenvalues give L^2 and B^2 from the dimensionless form $\widehat{\boldsymbol{S}}$. The two forces acting on the droplet in this model are the drag force by both the droplet and the continuous fluid, and the interfacial surface tension, both are assumed to be additive. The evolution of the dimensionless $\widehat{\boldsymbol{S}} = \boldsymbol{S}/D_0$ is described as (Maffettone & Minale, 1998):

$$\frac{d\widehat{\boldsymbol{S}}}{d\hat{t}} = Ca \cdot \left(\widehat{\boldsymbol{W}} \cdot \widehat{\boldsymbol{S}} - \widehat{\boldsymbol{S}} \cdot \widehat{\boldsymbol{W}}\right) - f_1 \cdot \left(\widehat{\boldsymbol{S}} - g\left(\widehat{\boldsymbol{S}}\right) \cdot \boldsymbol{I}\right) + Ca \cdot f_2 \cdot \left(\widehat{\boldsymbol{E}} \cdot \widehat{\boldsymbol{S}} + \widehat{\boldsymbol{S}} \cdot \widehat{\boldsymbol{E}}\right), \tag{16}$$

where $\boldsymbol{I}$ is the second rank unit tensor, with $\hat{t} = t/\tau$, and $\widehat{\boldsymbol{W}}$ and $\widehat{\boldsymbol{E}}$ are the dimensionless forms of the vorticity tensor $\boldsymbol{W}$ and deformation rate tensor $\boldsymbol{E}$, also the symmetric and asymmetric parts of the velocity gradient tensor $\boldsymbol{V}$, respectively:

$$\boldsymbol{W} = 0.5(\boldsymbol{V} + \boldsymbol{V}^T), \tag{17}$$

$$\boldsymbol{E} = 0.5(\boldsymbol{V} - \boldsymbol{V}^T). \tag{18}$$

where they are divided by $\dot{\gamma}$ for simple shear flow and $\dot{\varepsilon}$ for pure shear flow to make them dimensionless. The time scale τ (s) is:

$$\tau = \frac{\mu_C \cdot D_0}{2\gamma}. \tag{19}$$

Furthermore, to preserve the volume, $g(\widehat{\boldsymbol{S}})$ is defined as:

$$g(\widehat{\boldsymbol{S}}) = 3 \cdot \frac{III_{\widehat{\boldsymbol{S}}}}{II_{\widehat{\boldsymbol{S}}}}, \tag{20}$$

where $III_{\widehat{\boldsymbol{S}}}$ is the determinant of $\widehat{\boldsymbol{S}}$ and $II_{\widehat{\boldsymbol{S}}}$ is the second invariant:

$$II_{\widehat{\boldsymbol{S}}} = 0.5(tr(\widehat{\boldsymbol{S}})^2 - tr(\widehat{\boldsymbol{S}}^2)), \tag{21}$$

with $tr(\widehat{\boldsymbol{S}})$ denoting the trace of matrix $\widehat{\boldsymbol{S}}$. The coefficients f_1 and f_2 depend on the viscosity ratio λ and Ca number as follows:

$$f_1 = \frac{40(\lambda + 1)}{(2\lambda + 3)(19\lambda + 16)}, \tag{22}$$

$$f_2 = \frac{5}{2\lambda + 3} + \frac{3Ca^2}{(2 + 6Ca^2)}. \tag{23}$$

The model assumes steady-state in the deformation of the droplet which means that in each time point, the droplet reaches its maximum deformation. Therefore, $d\widehat{\boldsymbol{S}}/d\hat{t} = 0$ in Eq. 16 and is applied for the different flow regimes (for derivation of the following equations, see Appendix A). For simple shear flow ($\alpha = 0$), L and B are calculated by:

$$L^2 = \frac{{f_1}^2 + Ca^2 + f_2 \cdot Ca\sqrt{{f_1}^2 + Ca^2}}{({f_1}^2 + Ca^2)^{1/3} \cdot ({f_1}^2 + Ca^2 - {f_2}^2 \cdot Ca^2)^{2/3}}, \tag{24}$$

$$B^2 = \frac{{f_1}^2 + Ca^2 - f_2 \cdot Ca\sqrt{{f_1}^2 + Ca^2}}{({f_1}^2 + Ca^2)^{1/3} \cdot ({f_1}^2 + Ca^2 - {f_2}^2 \cdot Ca^2)^{2/3}}, \tag{25}$$

and for pure shear flow ($\alpha = 1$):

$$L^2 = \frac{f_1 \cdot g(\widehat{\boldsymbol{S}})}{f1 - 2Ca \cdot f_2}, \tag{26}$$

$$B^2 = \frac{f_1 \cdot g(\widehat{\boldsymbol{S}})}{f_1 + 2Ca \cdot f_2}, \tag{27}$$

where:

$$g(\widehat{\boldsymbol{S}}) = \left(\frac{{f_1}^2 + 4Ca^2 \cdot {f_1}^2}{{f_1}^2}\right)^{1/3}. \tag{28}$$

Finally, the general case with varying α is calculated by:

$$L^2 = \left(\frac{\hat{S}_{11} + \hat{S}_{22}}{2}\right) + \sqrt{\left(\frac{\hat{S}_{11} + \hat{S}_{22}}{2}\right)^2 - \hat{S}_{11} \cdot \hat{S}_{22} + {\hat{S}_{12}}^2}, \tag{29}$$

$$B^2 = \left(\frac{\hat{S}_{11} + \hat{S}_{22}}{2}\right) - \sqrt{\left(\frac{\hat{S}_{11} + \hat{S}_{22}}{2}\right)^2 - \hat{S}_{11} \cdot \hat{S}_{22} + {\hat{S}_{12}}^2}. \tag{30}$$

where $\hat{S}_x$ denotes the matrix positions of $\widehat{\boldsymbol{S}}$.

2.2.3 The Lamb model

The Lamb model is based on how the shape of the droplets oscillate when influenced by forces and how it is damped by viscous effects (Lalanne et al., 2019). Viscous droplets oscillate in different eigenmodes (n) with specific angular frequencies (ω_n) and damping rate (β_n) which gives different droplet shapes where the second mode has been shown to be most prominent and create an elliptical droplet shape (Lalanne et al., 2019; Rayleigh, 1879; Risso & Fabre, 1998). The model is defined as (Lalanne et al., 2019; Risso & Fabre, 1998):

$$\frac{d^2A}{dt^2} = K \cdot F(t) - 2\beta_2 \cdot \frac{dA}{dt} - {\omega_2}^2 \cdot A, \tag{31}$$

with oscillation mode 2 where A is the oscillation amplitude, K is a dimensionless constant and $F(t)$ is the turbulence forcing term:

$$F(t) = \frac{We(t) \cdot \gamma}{{D_0}^2 \cdot \rho_C}. \tag{32}$$

With $X = (\beta_2/\omega_2)$, together with We, Eq. 31 can be written in dimensionless form:

$$\frac{d^2\hat{a}}{d\hat{t}^2} = K \cdot We(t) - 2\mathrm{X} \cdot \frac{d\hat{a}}{d\hat{t}} - \hat{a}, \tag{33}$$

where $\hat{t} = (t \cdot \omega_2)$. By solving A in Eq. 31, the length L at a given time t is given by:

$$L = D_0 + 2A(t). \tag{34}$$

The damping rate β_n and the frequency ω_n can be calculated in different ways and four methods are compared: the Lamb-, Miller-Scriven-, Lalanne- and Roa-method (Lalanne et al., 2019; Lamb, 1993; Miller & Scriven, 1968; Roa et al., 2023). For the full equations, see Appendix B.

2.3 The Courant number

When the time dimension is introduced to CFD simulations, the temporal resolution of the simulation must be considered. The timesteps, Δt, of a time-resolved CFD simulation should be small enough that the simulated fluxes do not traverse several control spaces in one step. The Courant number, Co, is a dimensionless number that describes the relation between temporal and spatial resolutions in a transient flow simulation. It is, generally, the quotient of the distance traversed by the flow in one time step over the length of the control space. The Courant number is defined as follows,

$$Co = \frac{v \cdot \Delta t}{\Delta l}. \tag{35}$$

Where v is the fluid velocity and Δl the length of the control space and Δt is the time step length. In a time-dependent transient fluid simulation it is desirable to use sufficiently small-time steps so that the maximal Co of the system is smaller or equal to one (Talimi et al., 2012). Eq. 35 is the defined equation for the Co number in one-dimension. There are other methods to calculate the Co number in two-dimensional or three-dimensional control spaces of varying geometries. In this study the Co number is computed by ANSYS Fluent 2025 R1 for two-dimensional control spaces.

3 Material and Methods

This section describes the investigation of drop deformation in three parts. The first part consists of extraction and analysis of the drop deformation data from the experimental trials. This includes a description of the geometry, fluid phase properties and image processing. The empirical data is then used to evaluate the three deformation models; Weber, MM and Lamb, based on the 1D DPM data. Lastly, a 2D VoF simulation is conducted.

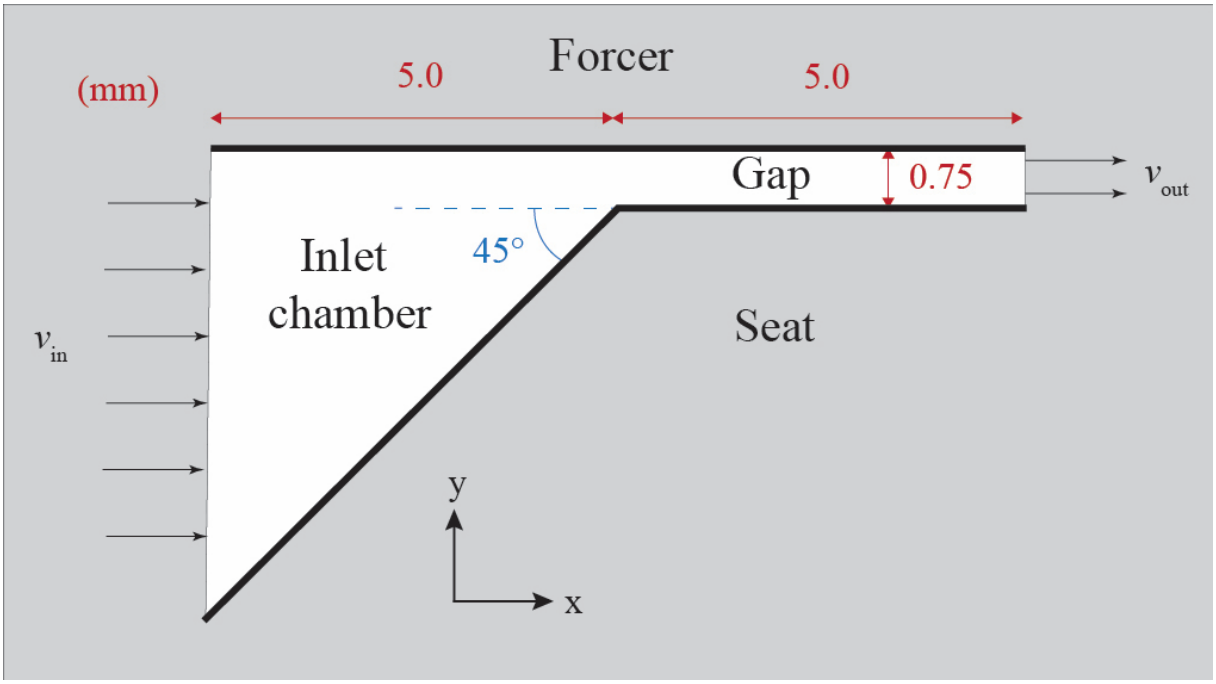

Figure 4: illustration of the inlet chamber and gap of a lab-scale HPH valve with velocity in, v_{in} and out, v_{out}, gap inlet measured from the inlet boundary to 5.0 mm, gap length $L_g = 5.0$ mm, gap height, $h = 0.75$ mm, and gap inlet radius $\Lambda_\alpha = 45°$.

3.1 Experimental valve model

A cuboid and planar flow-cell, modelling the cross-sectional geometry of the forcer-seat inlet chamber of a HPH valve, was constructed (Håkansson, 2025). In summary the flow cell characteristics were as follows. The incline of the sloped wall approaching the gap was $\Lambda_\alpha = 45°$, $h = 0.75$ mm as shown in Figure 4, and 7.5 mm as out-of-plane depth. A continuous phase of water was passed through the flow-cell and a disperse phase of food grade oil (Miglyol® 812, Caesar & Loretz, Hilden, Germany) with $\mu_D = 25$ mPa·s and $\rho_D = 950$ kg·m^{-3} was injected through a needle into the continuous fluid flow. The disperse phase was coloured with Nile red. The continuous phase was water with $\mu_C = 1.003$ mPa·s, yielding $\lambda = 25$. The flow was continuously monitored with a highspeed camera. The raw data used in this study was supplied directly by Andreas Håkansson, who constructed and operated the original device. The raw data consisted of image series of trials with varying flow rates (Q): 1.03, 1.31 and 1.56 L·min^{-1}.

Drop release events were automatically identified using a python-based image processing algorithm. Image refinement and binarisation was carried out with the OpenCV 4.14.0 (cv2) package while drop identification was based on the regionprops function from sci-kit image 0.26.0 (skimage). Drop events with a minimum of 20 consecutively identified droplet images were collected from each data set. Subsequently, a Locally Weighted Scatterplot Smoothing (LOWESS) filter was implemented in python with the nonparametric.smoothers_lowess.lowess function from the statsmodel python package. The LOWESS-filtering was conducted with 10% data fraction on one iteration. To calculate the Ca number, the axial and radial velocity gradients are defined as (Håkansson, 2024):

$$\left|\frac{dv_x}{dx}\right| \approx \left|\frac{dv_y}{dy}\right| = (0.016 + 0.011\Lambda_\alpha) \cdot \frac{U_g}{h}, \tag{36}$$

where U_g is the average gap entrance velocity (m·s^{-1}). With $\Lambda_\alpha = 45°$, both (dv_x/dx) and (dv_y/dy) equals approximately $0.5 \cdot U_g/h$ so that Eq. 5 yields:

$$G = \frac{U_g}{h}. \tag{37}$$

3.2 DPM CFD modelling

For the deformation models, a steady-state Discrete Phase Model (DPM) was set up in ANSYS Fluent 2025 R1 on the geometry described in section 3.1. The Reynolds Averaged Navier-Stokes (RANS) method of turbulence modelling and the realisable k-ε viscosity model were used as per best practice recommendations of Olad et. al (2022a). Note that while Olad et. al concluded that the Renormalisation Group RNG k-ε viscosity model is more accurate than the realisable k-ε model, in general, the former underperforms under contracting flows (Altair, 2021). Thus, motivating the choice of the realisable k-ε viscosity model.

Uniform velocity inlet boundary condition with 2% turbulence and 0.1 turbulent viscosity ratio was used with $v_{in} = 0.398$ m·s^{-1}, 0.506 m·s^{-1} and 0.603 m·s^{-1}, respectively, to achieve approximately the same v at the gap inlet as the three experimental cases and yield $Q = 1.03$, 1.31 and 1.56 L·min^{-1}. The outlet was modelled as a pressure outlet with zero-gauge pressure, and wall treatment was set to enhanced with no-slip boundary condition. Second order accuracy was applied to all simulations. The influence of gravity was not simulated.

A group injection was made in ANSYS with 3 inert particles with the same properties as the disperse phase in the experiments with $D_0 = 0.10$ mm injected 1 mm from the inlet evenly spread between y-position 2 and 5 mm. Likewise, the continuous phase were given the same properties as in the continuous phase in the experimental valve method. The velocity gradient data for each particle track were exported from ANSYS Fluid. For the DPM simulations, $D_0 = 0.10$ mm was chosen to generate a trajectory similar to the experimental observed trajectories. Furthermore, it was assumed that the particles were small enough to have the same velocity profiles as the continuous fluid.

3.3 Governing equations for deformation modelling from 1D DPM data

For the deformation models, the same parameters were used as the experimental setup while the material properties of $\lambda = 25$, $\mu_C = 1.003$ mPa·s^{-1} and $\gamma = 13$ mN·m^{-1} were supplied directly Andreas Håkansson who conducted the original physical experiments. The velocity gradient data for the mathematical models were obtained from the particle injection explained in section *3.2* and used to calculate the Ca number for each model by Eq. 5.

For the Weber model, Eq. 12 was solved for L in python using the scipy method solve_ivp with the Backward Differential Formula (BDF) algorithm. This algorithm was used for all models since the ODEs contain multiple state variables with varying time constants which may require smaller time steps (Bui & Bui, 1979). With $We_d = 0.42$ for $\lambda = 0.002$ retrieved from Innings et al. (2015), We_d was calculated to 0.36 with λ = 25 by the relationship in Eq. 15. From the boundary condition of constant volume for the droplet, B was calculated by:

$$B = \sqrt{\frac{{D_0}^3}{L}}. \tag{38}$$

The optimal dynamic Weber number, $We_{d,opt}$, was evaluated to give the same L/B as the LOWESS-filtered empirical data by using the scipy.optimize.minimize function in python with the Nelder-Mead method and a tolerance of 0.0001 and $We_d = 0.36$ as the guess.

For the MM model, the L and B were solved analytically by the means of Eq. 24 and 25 for simple shear flow ($\alpha = 0$), Eq. 26 and 27 for pure shear flow ($\alpha = 1$), and numerically by Eq. 29 and 30 for general flow with varying α with the scipy.optimize.root function with the "hybr" method in python.

For the Lamb model, Eq. 33 was converted to a first order ODE by setting $d\hat{a}/d\hat{t} = E$:

$$\frac{d\hat{a}}{d\hat{t}} = K \cdot We(t) - 2X \cdot E - \hat{a}, \tag{39}$$

where L was calculated from Eq. 34 and subsequently B from Eq. 38 where β_2 and ω_2 were calculated by four different methods (see Appendix B) to yield X, and K was set to $1/25$ as suggested by Håkansson (2022). The deformation ratio L/B for the different deformation models were then compared.

3.4 Meshing and mesh independence

A flow geometry was constructed in ANSYS 2025 R1 DesignModeler as illustrated in Figure 4. A rough mesh was generated using ANSYS 2025 R1 Meshing, mainly quadrilateral with an average lattice length of 0.2 mm and further mesh refinements were carried out in ANSYS Fluent. The droplet deformation, L/B, derived by the Weber model was selected to

study mesh dependence (see Appendix C). At a lattice length of 12.5 μm with a near-wall lattice length of 6.25 μm no significant change in deformation was achieved by finer meshes.

3.5 2D VoF deformation modelling

A transient two-phase system was modelled with the Multiphase (Volume of Fluid) method in ANSYS Fluent, utilising the same flow geometry, turbulence model and viscosity model as described in section 3.2. In addition to the aqueous phase, here implemented as the continuous phase, an immiscible oil phase was also implemented with $\rho_D = 950$ kg·m^{-3} and $\mu_D = 25$ mPa·s. The phase interface was set to sharp with anti-diffusion and the interfacial tension was modelled as a continuous surface force with the interfacial tension coefficient $\gamma = 13$ mN·m-1. All simulations were carried out with double precision, enhanced wall treatment and no-slip wall boundary conditions.

Uniform velocity inlet boundary condition was used to achieve the same volumetric flow rate at as the experimental scenarios and the outlet was modelled as a pressure outlet. During the simulation, snapshots were taken of the phase-contours with regular intervals. The images were then processed with the same image processing algorithm as developed for the experimental valve model.

A mesh dependence study was also carried out comparing the droplet deformation, L/B between different mesh densities, further explained in Appendix C. However, complete mesh independence was not achieved as L/B diverged significantly after the gap inlet between all studied mesh densities. The finest mesh examined had an average lattice length of 6.25 μm and total cell count of ~300k. Finer meshes were considered but were deemed unfeasible due to hardware limitations. Timestep lengths were chosen for each mesh density in order to limit the Co number to below one.

The oil phase was initialized into the model as a homogenous circular region with a diameter of 0.5 mm and centroid position x = 1.75 mm, $y = 4.7$ mm. This setup together with an inlet velocity, $v_{in} = 0.506$ m·s^{-1} corresponding to $Q = 1.36$ L $\cdot$ min^{-1}, was used to test the viability of the method and to conduct the mesh dependence study. During the study, it also became apparent that all mesh densities significantly overestimated the degree of deformation, and thus conducting the simulations with $\gamma = 13$ mN·m^{-1} was deemed inviable. An effective interfacial tension coefficient, γ_{eff}, was introduced as a simple multiple of γ. The γ_{eff} was then empirically determined to 16γ for this setup. A possible explanation for this increase are missing physics errors introduced when a three-dimensional droplet is simulated only in two-dimensions, for a more in-depth discussion see Appendix C. The introduction of γ_{eff} also decreased the mesh dependency of the simulation, although complete mesh independence was not reached (see Appendix C). Lattice length 25 μm was chosen as the basis for further simulations.

VoF simulation using lattice length 25 μm and $\gamma_{eff} = 16\gamma$ were conducted for the three flow rates and nine initial diameters presented in Table 1, based on results from the experimental valve method. Each flow rate was paired with three initial droplet diameters totalling nine simulations. The initial centroid position was set to x = 1.75 mm and y = 4.7 mm, as before.

4 Results and discussion

This section presents and discusses the results regarding how the 1D DPM and VoF simulations correlate to the empirical data. The areas discussed are, in order; visualisation of the deformation within the experimental model, the 1D DPM simulations together with the Weber-, MM- and Lamb model, and the VoF simulations. Finally, implications for industrial scale HPH valves are discussed.

4.1 Experimental measurements of drop deformation

The initial droplet diameter, D_0, distributions for the different flow scenarios are presented in Figure 5. The distributions show that D_0 decreases with increasing Q. This phenomenon is expected since the oil droplet formation is dependent on the flow rate of the continuous phase passing the injection needle. Higher flow rates will decrease the droplet formation time by dislodging the nascent droplet from the injection needle faster.

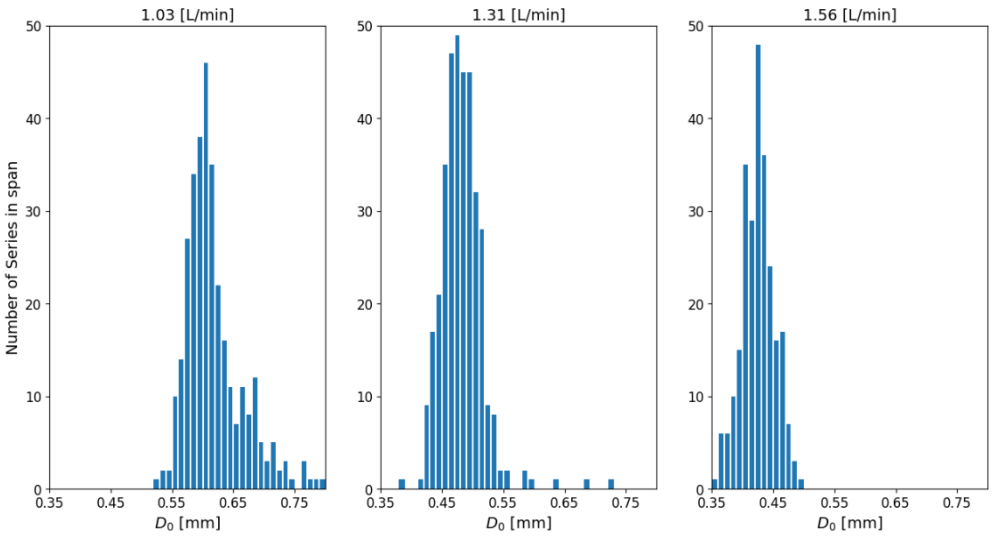

Figure 5: Distributions of D_0 for the three different flow rates left to right; $Q = 1.56$, 1.31 and 1.03 L·min^{-1}, respectively. The bars represent the number of observed drop events within each span of D_0, only drop events with at least 20 consecutive images were considered.

The difference in D_0 is important since larger droplets are more prone to deformation. Slower flowrates produce larger droplets as seen in Figure 5, which explains the different degrees of deformation between flowrates as seen in Figure 6. The degree of deformation decreases with increasing flowrates, due to decreasing droplet diameters. The scatterplot and corresponding LOWESS filtered curve are presented in

for all three flow rate series.

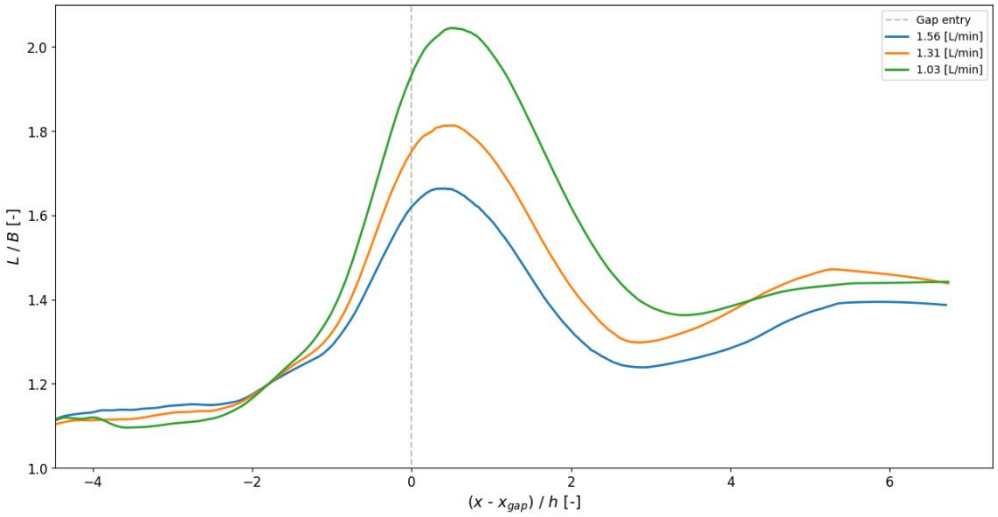

Figure 6: Drop deformation L/B of the 10% LOWESS-filtered empirical data for $Q = 1.03$ (green), 1.31 (orange) and 1.56 (blue) L·min^{-1}. The x-axis represents the horizontal distance of the fluid cell and is measured in gap heights, $(x - x_{gap})/h$, with 0 being the position of the gap inlet.

The elongational behaviour for the three different Q in Figure 6 are similar in shape, with axial elongation starting approximately two gap lengths before the gap entry (x_{gap}) and reaching the maximum L/B within one gap length after passing x_{gap}. The oil droplets proceed to contract after x_{gap} yet maintaining a slightly elevated degree of deformation upon exiting the chamber at approximately 6.7 gap heights (5 mm) after the gap inlet. The second peak in deformation could be explained by the laminar flow profile in the narrow gap causing greater shear-rates. The L/B maxima of the LOWESS-filtered data are 1.66, 1.81 and 2.05 for $Q = 1.56$, 1.31 and 1.03 L·min^{-1}, respectively.

The different flow rates were subdivided into three subpopulations each depending on D_0. The average of these subgroups, $\overline{D_0}$, will be used in further modelling. The initial diameter span, $D_{0,span}$, for three data series and their corresponding $\overline{D_0}$ are shown in Table 1. Note that almost all scenarios have a $\overline{D_0} > h/2$, with only 7 out of 907 drop release events having a $D_0 < h/2$. The relatively large size of the droplets compared to the gap height suggests that the droplets may experience physical deformation by the walls, as suggested by Innings (2011).

Table 1: Initial diameter span, $D_{0\,span}$, and average, $\overline{D_0}$, for the three data series with different flow rates Q, and their respective standard deviation, std, and number of drop series, n. The droplet diameter as a fraction of the flow cell gap height h (0.75 mm) is also shown.

Q [L·min^{-1}]	$D_{0,span}$ [mm]	$\overline{D_0}$ [mm]	$2{\cdot}std$ [mm]	$\overline{D_0}/h$ [%]	n [-]
1.03	(0.50, 0.58)	0.57	0.0031	76%	56
	(0.58, 0.62)	0.60	0.0031	80%	153
	(0.62, 0.72)	0.66	0.0056	88%	100
1.31	(0.38, 0.45)	0.44	0.0030	59%	49
	(0.45, 0.52)	0.48	0.0022	64%	281
	(0.52, 0.75)	0.56	0.0200	75%	27
1.56	(0.35, 0.40)	0.39	0.0025	52%	25
	(0.40, 0.45)	0.42	0.0020	56%	172
	(0.45, 0.50)	0.47	0.0033	63%	44

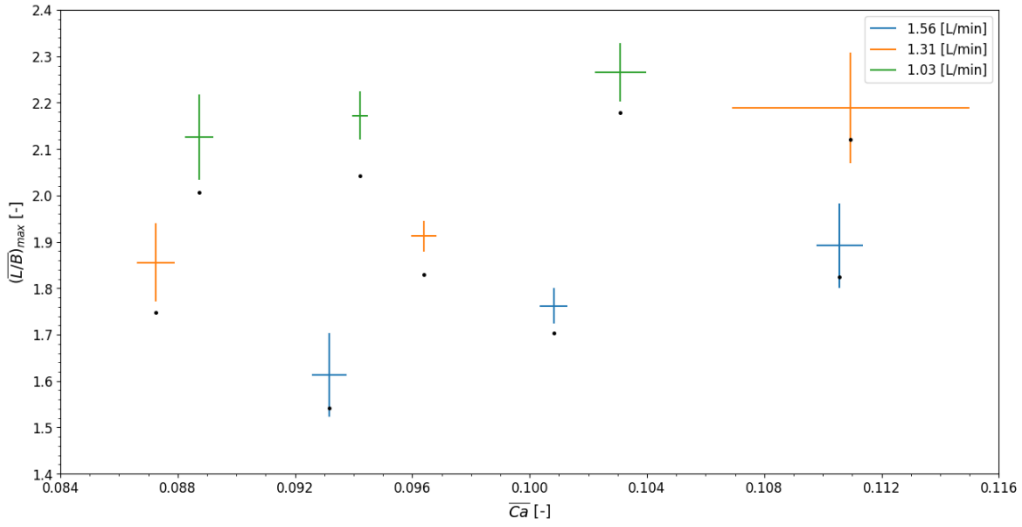

Figure 7: Maximum deformation $(\overline{L/B})_{max}$ and average Capillary number $\overline{Ca}$ for the subseries based on initial droplet diameter, described in Table 1. The vertical and horizontal bars show the confidence interval, with 95% confidence, for $(\overline{L/B})_{max}$ and $\overline{Ca}$ respectively. Three different flow rates are depicted: Q = 1.56 (blue), 1.31 (orange) and 1.03 (green) L·min^{-1}. The black dots represent the maxima of the 10% LOWESS curve for each subseries.

4.2 Inlet chamber velocity gradients

The velocity gradient is the CFD-derived parameter that affects the deformation in the mathematical models. Figure 8 shows the particle trajectories for the three flow scenarios. For the 1D DPM simulations, D_0 was set to 0.10 mm for the particle trajectories to imitate the experimental LOWESS-filtered trajectories in Figure D1. This D_0 is different from the experimental $D_{0,span}$ because the particles hit the wall in the simulations for $D_0 = 0.35$ mm (the lowest $\overline{D_0}$) as shown in Figure E1. The DPM method considers the particles as point objects and the trajectories show the centroid positions of the droplets. The radius of the particles affects their trajectories and since the centroid positions of a 0.35 mm droplet collides with the wall, it suggests infinite deformation which is not probable. This shows a limitation of using 1D DPM simulations for comparatively large droplets.

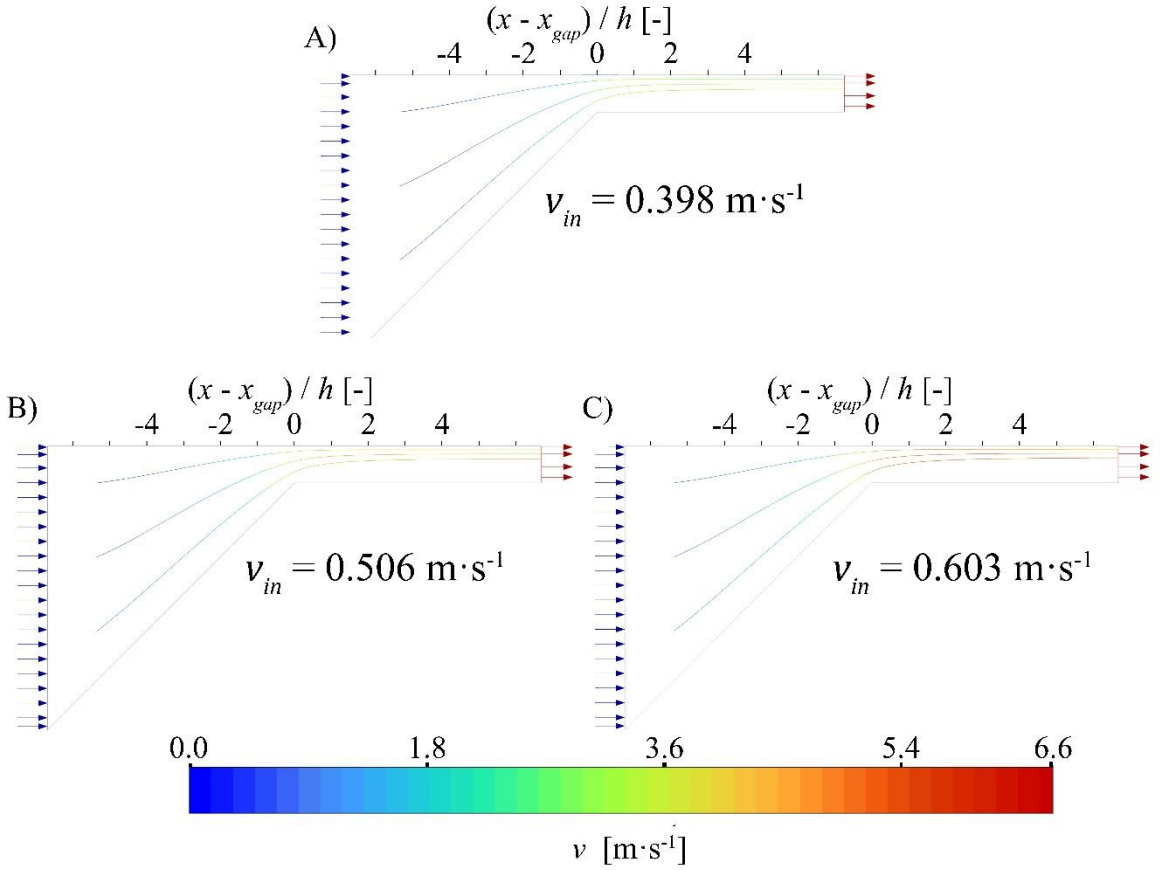

Figure 8: Particle trajectories for (A) $v_{in} = 0.398$ m·s^{-1} ($Q = 1.03$ L·min^{-1}), (B) $v_{in} = 0.506$ m·s^{-1} ($Q = 1.31$ L·min^{-1}) and $v_{in} = 0.603$ m·s^{-1} ($Q = 1.56$ L·min^{-1}). The particles where set with $D_0 = 0.10$ mm, $\rho_D = 950$ kg·m^{-3}, 1 mm from the inlet and evenly spread between y=2 and y=5. The colour gradient represents the velocity magnitude for the continuous phase.

The velocity gradient for the particle tracks are shown in Figure 9. The solid, dashed and dotted lines represent the particle trajectories for particle ID 0, 1 and 2, respectively. It shows an increase in maximum G with increasing Q, and that particle ID 2 experiences the highest G. This means that the G is the highest at the seat edge compared to the forcer wall. It also shows that the G is the highest right before the gap inlet.

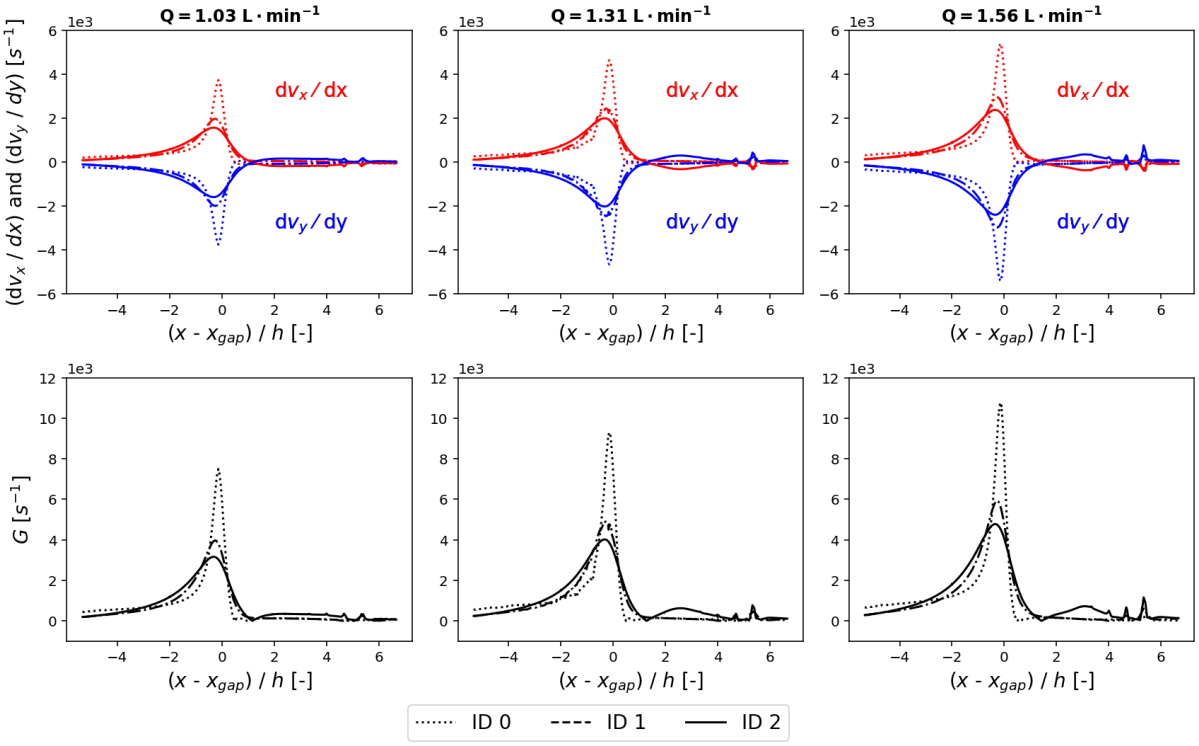

Figure 9: Velocity gradients along the x-axis and y-axis (upper row) and the absolute sum of these (G) (lower row) for particle ID 0, 1 and 2 for three different flow rates; $Q = 1.03$, 1.31 and 1.56 L·min^{-1}. The particles had $D_0 = 0.10$ mm, $\rho_D = 950$ kg·m^{-3} and were set 1 mm from the inlet and evenly spread between $y = 2$ and $y = 5$.

4.3 Drop deformation based on the 1D DPM velocity gradients

The drop deformations L/B from the mathematical models presented in Figure 10 are based on the trajectories in Figure 8. The red solid, dash-dotted and dashed lines represent the MM-model for pure shear flow, complex flow and simple shear flow, respectively. The solid green lines and blue dash-dotted lines represent the Weber model and Lamb model, respectively. As comparison, the dashed black lines represent the LOWESS-filtered empirical data. Note that the Weber- and Lamb model are dynamic while the MM-model assumes steady-state, and the CFD simulation assumes steady continuous phase flow, and the L/B is calculated based on the velocity gradients in the centre of the droplets.

Both the Weber model and the MM-model with pure shear flow behave in a similar way as the empirical data for ID 1 and 2. Particle ID 0 shows the highest deformation and can be explained by its trajectory being closest to the seat edge where G is the highest (Figure 9). The trajectory for ID 2 shows a second peak close to three h after the gap. One reason could be that this particle track is close to the upper wall where the velocity is lower compared to the middle (see Figure E2), which causes an increase in G. Since the lowest D_0 is 0.35 mm, this trajectory would cause the theoretical radius to overlap with the wall which is physically unrealistic.

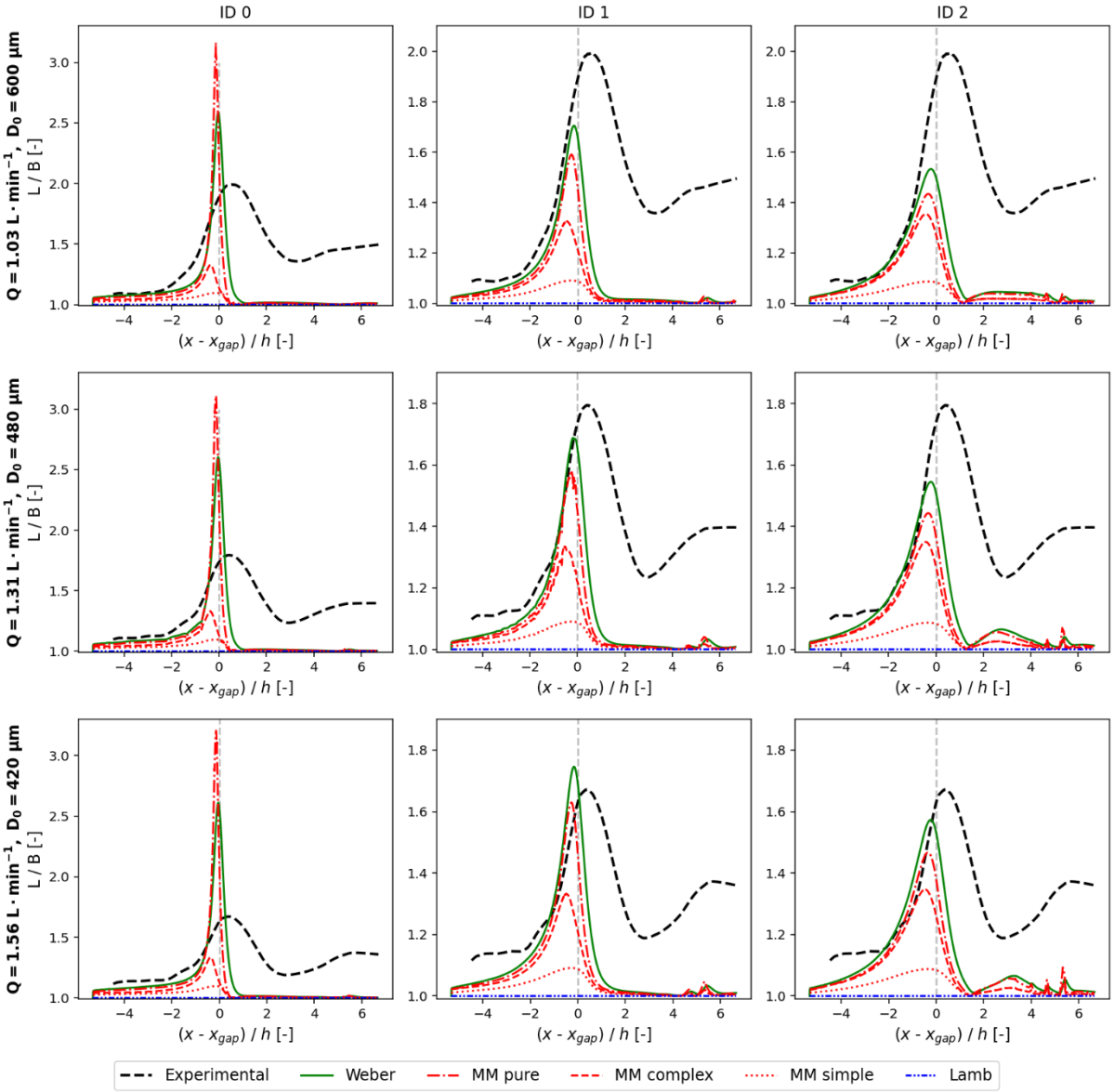

Figure 10: Drop deformation L/B for different particle IDs along the trajectories. The upper row represents $D_0 = 0.60$ mm and $Q = 1.03$ L·min^{-1}, the middle row represents $D_0 = 0.48$ mm and $Q = 1.31$ L·min^{-1}, and the lower represents $D_0 = 0.42$ mm and $Q = 1.56$ L·min^{-1}. L/B was calculated for the Weber model (green), MM model (red) for pure shear, simple shear and complex flow, and Lamb model (blue) and compared to the LOWESS-filtered empirical data (black).

The Lamb model, however, showed significantly lower deformation than the other two models and did not correlate to the empirical data. Figure 11 shows how the different methods to calculate β_2 and ω_2 affects the deformation prediction. It shows that the Lalanne- and Lamb-method behave similarly and converge towards the same amount of deformation while the other two deviate.

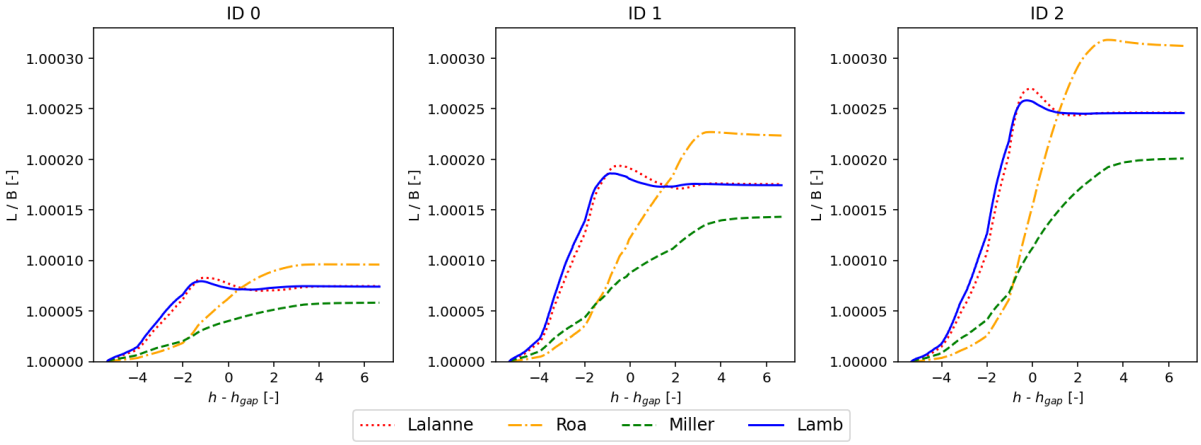

Figure 11: Drop deformation L/B for the Lamb model for the particle track ID 0, 1 and 2 with four different methods to calculate β_2 and ω_2: Lalanne method (red), Roa method (orange), Miller-Scriven method (green) and Lamb method (blue). The L/B was calculated with $D_0 = 0.48$ mm in the equations with velocity gradients from the trajectories with $v_{in} = 0.506$ m·s^{-1} ($Q = 1.31$ L·min^{-1}).

Particle ID 1 travelled the closest to the middle of the gap inlet and had the most similar particle trajectory as the trajectory for the LOWESS-filtered empirical data (for trajectories, see Appendix E and Figure 8). It was therefore chosen to compare deformation with different D_0 and Ca numbers. Figure 12 shows the L/B for particle ID 1 for the mathematical models and the LOWESS-filtered empirical data for the three flow scenarios. It shows a trend of higher deformation with higher D_0, as expected, and the Weber model shows the most similar maximum L/B as the empirical data, especially for $Q = 1.31$ L·min^{-1} (see Table 2). Furthermore, both the Weber- and MM-model follows the experimental deformation trend well up until ~0.5 h. It is also seen that the MM-model has the most similar maximum L/B for $Q = 1.56$ L·min^{-1}.

Regarding the MM-model, the flow type α ranges were (0.49, 0.77), (0.51, 0.78) and (0.47, 0.77), for $Q = 1.03$, 1.31 and 1.56 L·min^{-1}, respectively. Although this suggests that the complex flow MM-model is more appropriate, the pure shear flow assumption aligns with the empirical data the most. This shows that the model lacks some physical phenomena. For easier visualisation, only the pure shear MM-model is shown in Figure 12.

Figure 12 shows a trend of higher deformation with higher D_0, as expected, and the Weber model shows the most similar maximum L/B as the empirical data, especially for $Q = 1.31$ L·min^{-1} (see Table 2). Furthermore, both the Weber- and MM-model follows the experimental deformation trend well up until ~0.5 h. It is also seen that the MM-model has the most similar maximum L/B for $Q = 1.56$ L·min^{-1}.

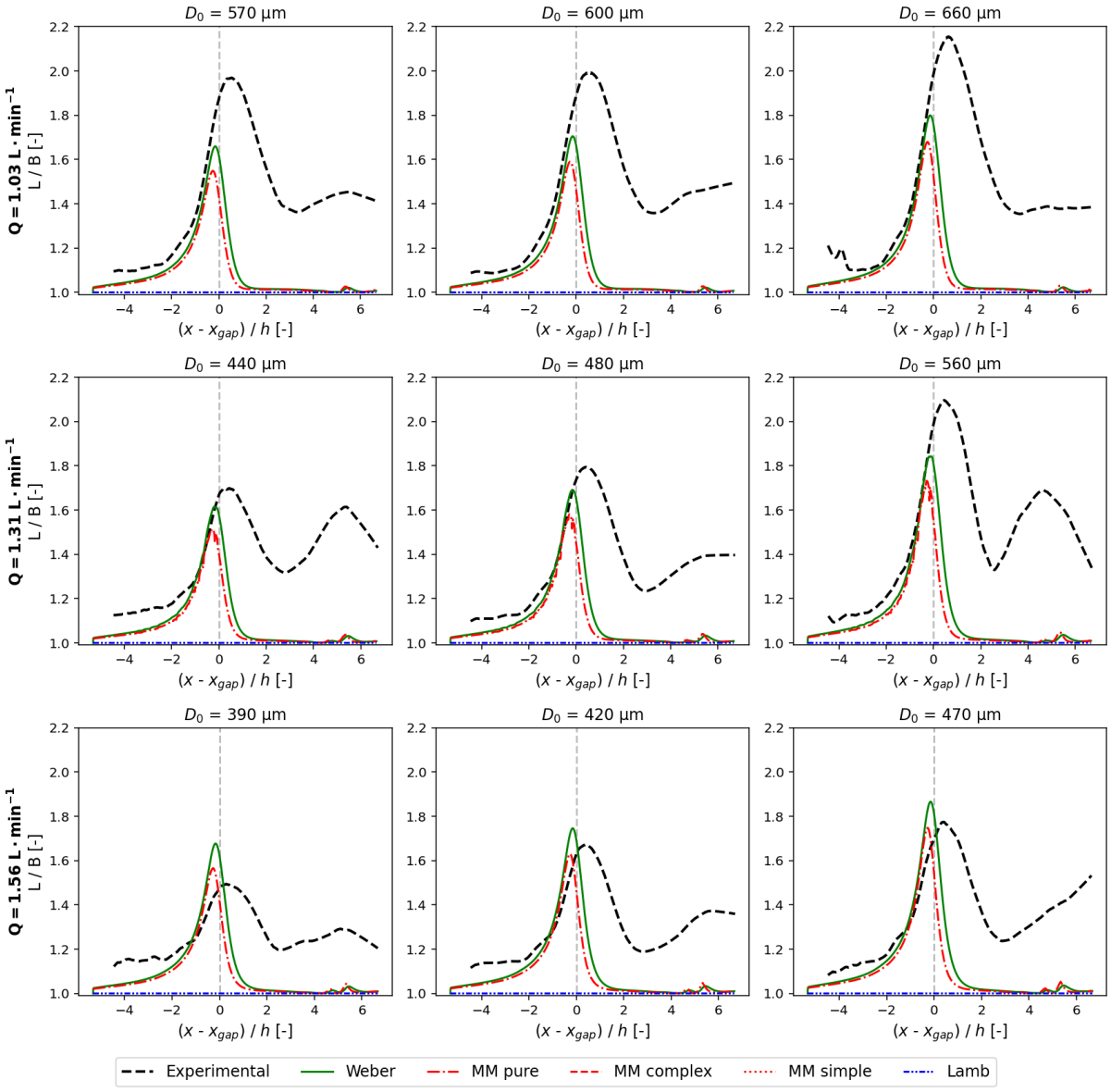

Figure 12: Drop deformation L/B for different D_0 along the trajectories for particle track ID 1. The upper, middle and lower rows represent $Q = 1.03$, 1.31 and 1.56 L·min^{-1}, respectively. L/B was calculated for the Weber model (green), MM model (red) and Lamb model (blue) and compared to the LOWESS-filtered empirical data (black).

The MM-model does not have any empirical parameters so the maximum deformation cannot be changed. However, the Weber model is based on the empirical constant We_d that was originally set to fit empirical data by Innings et al. (2005), and the $We_d = 0.36$ used here comes from the relationship in Eq. 15. Table 2 shows the optimised dynamic Weber number, $We_{d,opt}$, for the model to reach the same L/B as the LOWESS-filtered empirical data for different D_0 and Q. For comparison, the original difference between the maximum L/B between the LOWESS-filtered empirical data and the Weber model $\Delta(L/B)$ (%) is shown both for $We_d = 0.36$ and each $We_{d,opt}$. It shows that there is no We_d that fits all. However, the $We_{d,opt}$ is similar within each case of Q, except for $Q = 1.56$ L·min^{-1}, indicating that it might be flow-dependent.

Table 2: Difference of L/B between the empirical LOWESS-filtered data and the Weber model, $\Delta(L/B)$ with $We_d = 0.36$, and $\Delta(L/B)$ with the optimal dynamic Weber number, $We_{d,opt}$, that minimises $\Delta(L/B)$, for different Q and D_0.

Q [L·min^{-1}]	D_0 [mm]	$We_d = 0.36$ $\Delta(L/B)$ [%]	$We_{d,opt}$ [-]	$We_d = We_{d,opt}$ $\Delta(L/B)$ [%]
1.03	0.57	16	0.27	0.0016
	0.60	14	0.28	0.0015
	0.66	17	0.28	-0.014
1.31	0.44	4.9	0.33	-0.0042
	0.48	5.9	0.32	0.0092
	0.56	12	0.30	-0.016
1.56	0.39	-12	0.46	-0.0031
	0.42	-4.4	0.39	0.0055
	0.47	-5.1	0.39	0.0037

Both Figure 10 and Figure 12 shows that the mathematical models have their maximum points slightly before the gap inlet whereas the empirical data shows the maximum deformation right after. One explanation is that the droplets are relatively large with the smallest $D_0 = 0.35$ mm being >$0.5h$. When the centroid position of the droplet is at the gap inlet ($h = 0$), half the droplet is still subject to the high G before the gap (Figure 9), and the 1D DPM simulation does not take this into account. The D_0 in industrial HPHs vary between applications, but usually significantly smaller, with an average $D_0 = 3.4$ µm (Walstra, 1999, p. 108), which likely decreases this discrepancy.

Figure 13 shows how the Weber model (green), MM-model (red) and Lamb-model (blue) behave at different Ca numbers under the assumption that the Ca number scales with h. Furthermore, the LOWESS-filtered data and mean Ca number for each $D_{0,span}$ for the empirical data are presented together with previous research from Innings (2005). It is seen from Figure 13 that the Lamb model and MM model for simple shear and complex flow type do not fit any of the empirical data and are therefore considered irrelevant. The Weber- and MM-model, however, show a similar trend as the data points from both this study and Innings (2005), and the MM-model is in the similar area. Note that Innings used $\lambda = 70$ with $h = 0.0700$, 0.145 and 0.220 mm with D_0 between 5 and 50 µm, compared to $\lambda = 25$ and $h = 0.75$ mm and $\overline{D_0}$ between 390 and 660 µm for this study. Even though these parameters differ, the comparison is still interesting since these data points have similar Ca numbers to the data of this study.

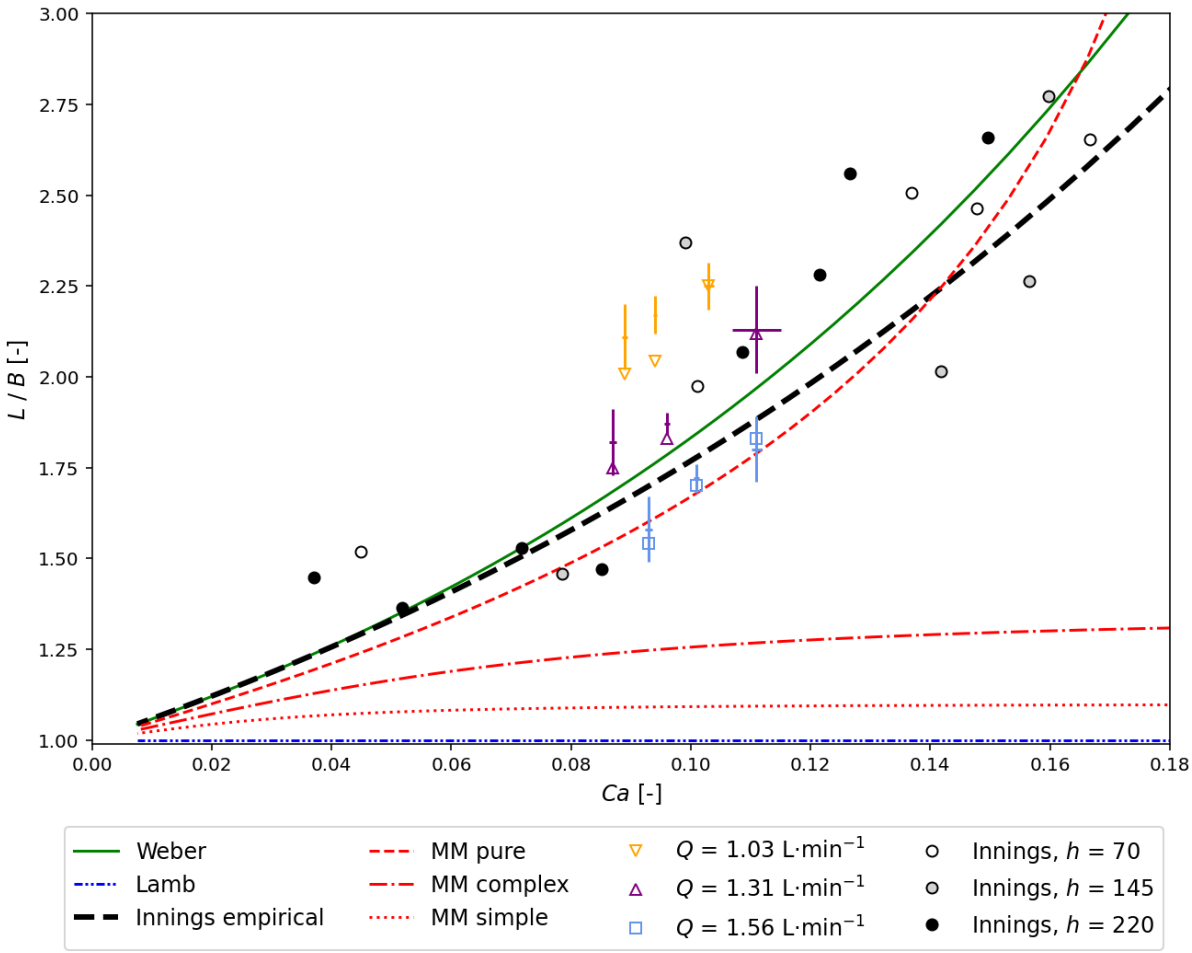

Figure 13: Drop deformation L/B for the mathematical models, the LOWESS-filtered data and empirical data from Innings (2005) for different Ca numbers. The LOWESS-filtered data is shown with $Q = 1.03$ (▽), 1.31 (△) and 1.56 (□) L·min^{-1}, together with the standard deviation spread of L/B and Ca for the non-filtered empirical data shown as vertical and horizontal lines, respectively. The Ca numbers for the mathematical models are based on the velocity gradient from particle ID 1 with $D_0 = 0.48$ mm for different Ca numbers.

Considering only the data points from this study, presented as (▽), (△) and (□) for $Q = 1.03$, 1.31 and 1.56 L·min^{-1}, respectively, the series have approximately the same Ca numbers but the trends are separated in the amplitude of L/B. This indicates that there is something other than the Ca number that affects drop deformation. For an empirical model, more data points with a wider span of Ca numbers are needed, which would require modifying the lab-model HPH-valve to allow a wider range of bubble diameters at differing flowrates.

The assumption for the MM-model is that it reaches steady-state. An industrial HPH valve can experience velocities of >100 m·s^{-1} through the gap (Olad et al., 2022b) which most likely would not allow the droplets to reach steady-state. Likewise, although the experimental setup used in this study has significantly lower velocities of 4 m·s^{-1} in the gap and >1 m·s^{-1} in the inlet chamber, this may not be a valid assumption. This would imply that the MM model over-estimates deformation. However, this is only seen for particle ID 0 which experiences the highest G (Figure 9) while the rest tend to underestimate the deformation.

4.4 VoF modelling

The 1D DPM simulations assume steady continuous phase flow and simulates how droplets flow in their respective centre point. This simplification reduces the computational power but does not take the physical volume into account. As seen in Figure E1, this causes some of the point particles to hit the wall which is not probable.

In VoF simulations the droplets have spatial resolution, and the shape of the phase-boundary is calculated iteratively at every time-step. Because of this, it could be argued that transient VoF simulations are more accurate. However, the maximum L/B is significantly higher with the original $\gamma = 13$ mN·m^{-1} compared to the LOWESS-filtered empirical data (Figure 14). It is hypothesised that there is an effective interfacial tension coefficient (γ_{eff}) that yields a deformation in the VoF simulation that fits the empirical data. For a more in-depth discussion of γ_{eff} see Appendix C.

It is seen in Figure 15 that increasing the γ with a factor of 16 to get $\gamma_{eff} = 208$ mN·m^{-1} gives an accurate prediction of L/B for $Q = 1.03$ and 1.31 L·min^{-1} but not $Q = 1.56$ L·min^{-1} which instead overestimates the deformation. This indicates that γ_{eff} could be flow-dependent, but more evaluations with different Q are needed to draw any conclusions. Furthermore, the positions of the maximum L/B are similar to the empirical data.

For this 2D VoF simulation, the software assumes a cylindrical shape of the droplet instead of the real-life elliptical shape. This implies a halving of the Laplace pressure, as shown in Appendix C, and could impact the simulation result. However, this does not explain why $16{\cdot}\gamma$ fits the data well which means that there is some physical phenomenon that the VoF simulation does account for. A 3D VoF simulation would mitigate the Laplace pressure discrepancy although it would require significantly more computational power.

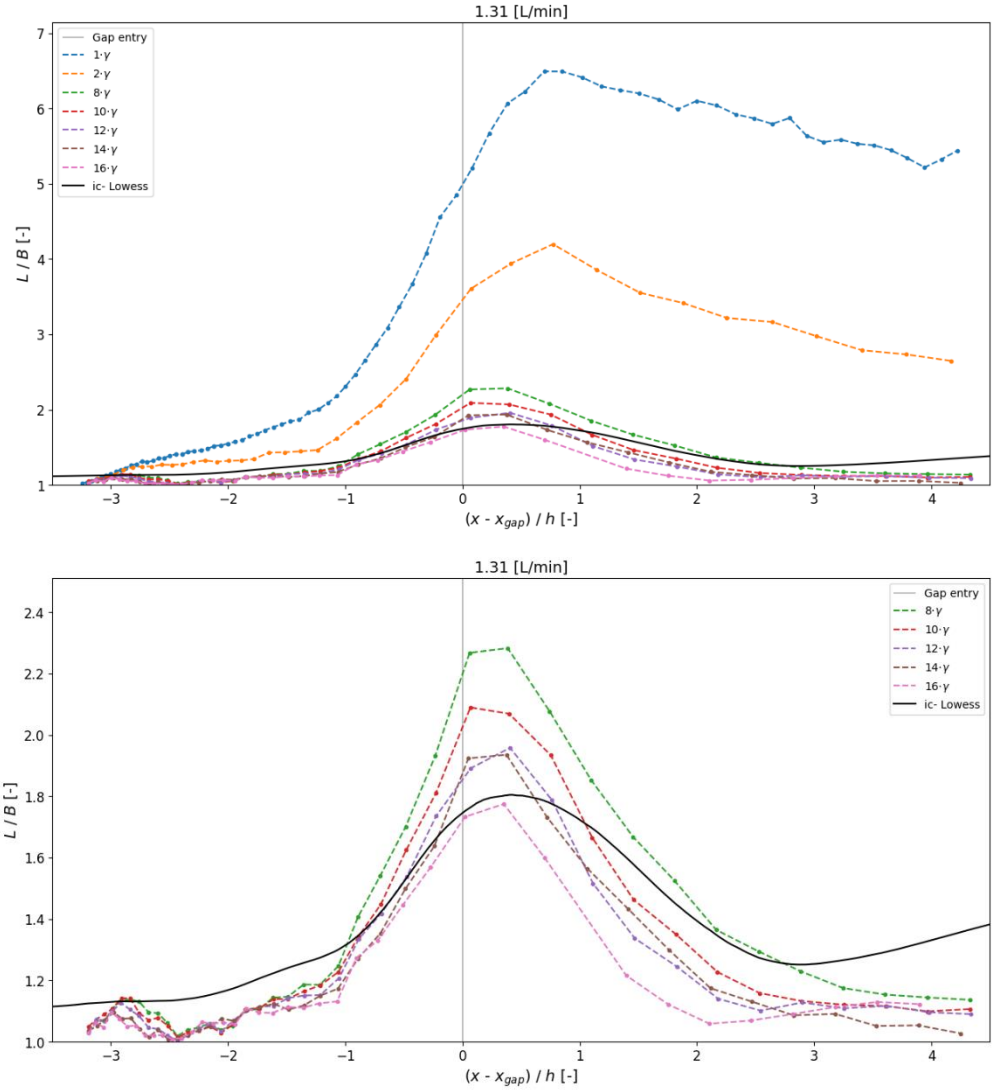

Figure 14: Drop deformation L/B for the droplets in the VoF simulations in ANSYS Fluid with $Q = 1.31$ L·min^{-1} and different γ_{eff}. The x-axis represents the horizontal distance travelled and is measured in gap heights, $(x - x_{gap})/h$, with 0 being the vertical location of the gap inlet. Blue, orange, green, red, purple, brown and pink dashed lines represent multiplicatives 1, 2, 8, 10, 12, 14 and 16 of the original $\gamma = 13$ mN·m^{-1}, respectively. Solid black line depicts the LOWESS-filtered curve of the experimentally observed oil droplet deformation for flow rate 1.31 L·min^{-1}. The upper figure includes all VoF γ-series while the lower figure excludes $1\cdot\gamma$ and $2\cdot\gamma$ for a clearer comparison with the LOWESS curve.

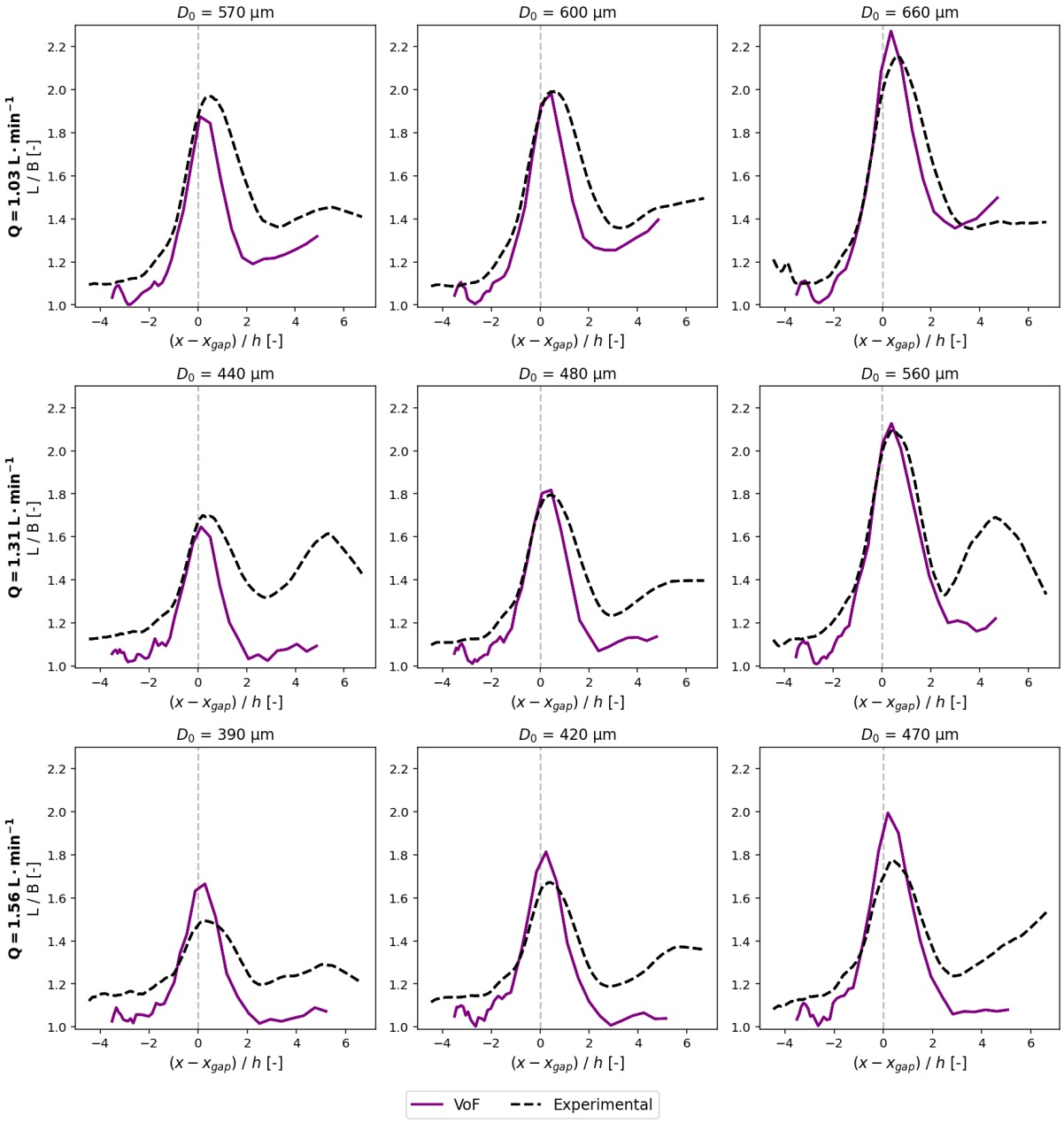

Figure 15: Drop deformation L/B for different D_0 for the VoF simulation (purple) and LOW-ESS-filtered empirical data (black) for $Q = 1.03$ (upper row) 1.31 (middle row) and 1.56 (lower row) L·min^{-1}. The VoF simulation data had $\rho_D = 950$ kg·m^{-3} and $\gamma = 208$ mPa·s.

As seen in Figure 16, the data points for the VoF are within similar ranges as the empirical data. Furthermore, the data points for $Q = 1.31$ and 1.56 L·min^{-1} follow a similar trend line while the data points for $Q = 1.03$ L·min^{-1} are separated in the magnitude of L/B. One explanation is that the VoF captures physical deformation for flows <1.31 L·min^{-1} where the droplets are larger. It is also note-worthy that the VoF-simulated deformation for $Q = 1.56$ L·min^{-1} consequentially overestimates deformation, likely due to a sub-optimal γ_{eff} fitting, with a γ_{eff} based on the higher flow rate it is probable that the VoF-method could capture the Ca-indpendent deformation also for the highest flow rate.

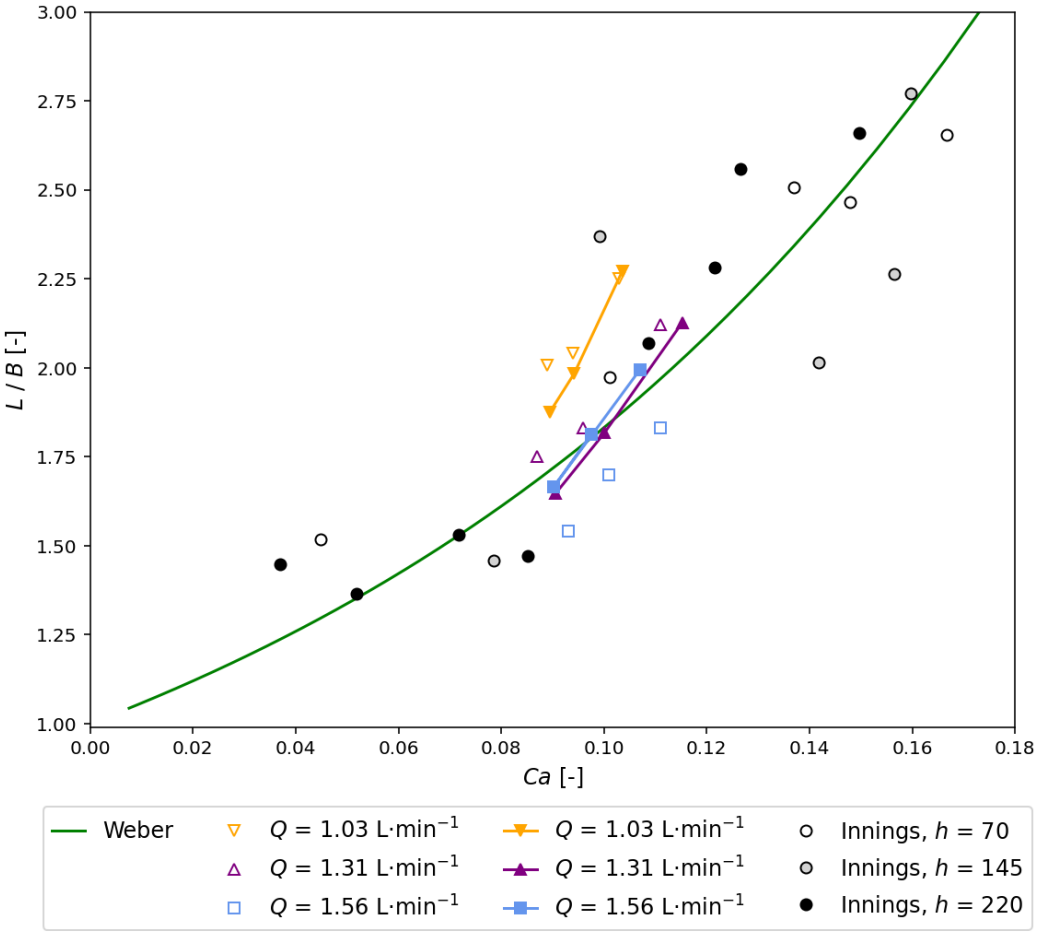

Figure 16: Drop deformation L/B for the VoF simulation, the LOWESS-filtered data and empirical data from Innings (2005) for different Ca numbers. The VoF (filled markers) and 10% LOWESS-filtered (non-filled markers) data are shown with $Q = 1.03$ (▽), 1.31 (△) and 1.56 (□) L·min^{-1}. The filled green line represents the Weber model.

4.5 Comparison of VoF and 1D DPM modelling

The positions of the maximum L/B for the VoF simulation fit well with the empirical data, while the corresponding positions for the 1D DPM models are slightly before the gap (see Figure 10, Figure 12 & Figure 15). This suggests that the 1D DPM data lacks physical effects present in the 2D VoF simulation. One explanation is that it does not account for spatial resolution.

The experimentally observed droplets are large compared to the gap inlet height 0.75 mm, with a $\overline{D_0}$ range of 0.39-0.66 mm. When the centroid position is at the gap inlet, there is still a part of the droplet within the region with high G. This is captured by the 2D VoF simulation, but not by the 1D DPM simulation. However, the VoF simulation also lacks physical effects since the 16 times higher γ_{eff} used to fit to the empirical data is not optimal for each case of Q.

Nonetheless, both methods predict the drop deformation well. The advantage with the 1D DPM simulation is that it requires significantly less computational power.

4.6 Implications for industrial-scale HPHs

This study considers a lab-scale HPH valve model and several parameters differ compared to an industrial scale HPH valve. Even though previous research has discussed that it is impossible to accurately scale all parameters (Innings et al., 2011), it is nonetheless interesting to evaluate how much the deformation behaviour theoretically differs.

The geometries and parameters for industrial scale HPHs differ and depend on the application. Typically, $r_i = 14$ mm and the Q can range from 10 000 to 50 000 L·h^{-1} and h can range from 0.13 to 0.37 mm (Håkansson, 2017; Innings & Trägårdh, 2007). With an average $D_0 = 3.4$ µm (Walstra, 1999, p. 108), this gives a Ca number span of $0.030 \leq Ca \leq 0.25$ compared to a span of $0.088 \leq Ca \leq 0.16$ in this study (see Figure 13) so that extrapolation is needed for the industrial scale HPH.

For further analysis, a wider Ca number span would be required to extrapolate towards the conditions of an industrial HPH-valve. Especially by decreasing droplet sizes which would also avoid squeezing effects. In the experimental setup described in this thesis, higher flow rates yield smaller D_0 and larger G. However, as seen in Eq. 5, the Ca number is proportional to the product of G and D_0 which means that they counteract each other, making it difficult to achieve wider Ca number span. Higher flow rates might also require other camera equipment with faster frame rates to capture the droplets.

One suggestion is to use a smaller needle and try with different positions of the needle. Another suggestion is to introduce a mixture of already dispersed droplets into the geometry. This could be achieved by first breaking the droplets in an initial homogenisation valve and measure deformation in a second inlet chamber. This could, however, make the droplet identification more complex since the droplets can break into several smaller fractions and clusters.

5 Conclusion

The aim of this thesis was to understand how emulsion droplet properties and device characteristics influence the deformation behaviour in a lab-scale HPH inlet valve and how it can be modelled. For this purpose, three objectives were formulated.

The first objective was to investigate drop deformation behaviour in a lab-scale HPH valve. Each data series with their respective volumetric flow rate Q show an increasing deformation trend with increasing Ca number. However, the magnitude of deformation differs between Q at comparable Ca numbers. This difference appears to be systematic with lower deformation at higher Q. This suggests that the Ca number does not capture the drop deformation on its own in this HPH valve setup. A possible explanation is squeezing due to the large relative size of droplets to gap height, with most droplets possessing a gap diameter greater than half the gap height. The Ca number does not account for the relationship between diameter and gap height.

The second objective was to investigate how well 1D DPM CFD simulations together with mathematical models can predict drop deformation. Out of the three deformation models, the Weber model and MM-model give good predictions of the extent of deformation L/B compared to the empirical data, both in magnitude and location in the x-axis.

The third objective was to investigate how well 2D VoF CFD simulations can predict drop deformation. This method requires an γ_{eff} 16 times higher than the real γ to reflect the behaviour in the experimental trials. This indicates that there is some physical effect that the VoF does not account for. With the fitted γ_{eff}, however, the VoF simulation predicts the deformation well although γ_{eff} seems to be flow dependent.

It is seen that both the 1D DPM and VoF simulations can be used to predict drop deformation well in this application. However, the 2D VoF method did not explicitly reproduce the observed difference in deformation magnitudes between all flowrates, independent of Ca numbers.

5.1 Future work

To build upon the findings of this study, several suggestions for future research are proposed. Firstly, it would be interesting to investigate how different inlet chamber geometries with differing inlet chamber angles Λ_α could affect the degree of deformation. Additionally, it is probable that the droplets in this study are large enough to be affected by physical deformation. Flow scenarios with smaller D_0 would decrease any squeezing effect and could give a wider Ca number span.

Furthermore, it is seen that the VoF simulation requires a significantly higher γ_{eff} than the real γ for the degree of deformation to fit the empirical data. γ_{eff} did also not fit the L/B for all the data sets and to validate if the γ_{eff} is flow dependent, a more extensive set of flow rates are needed. The value of γ_{eff} is empirically derived and lacks theoretical explanation. Investigating if there is a systematic relation of optimal γ_{eff} for different flow rates would thus be interesting. Conducting the VoF simulations in 3D may also indicate if the discrepancy is due to a missing physics error, when simplifying droplet physics to two-dimensional spaces.

6 References

Altair. (2021). *AcuSolve Training Manual - Theoretical background modeling of turbulence*. Altair Engineering Inc. Retrieved March 26 from https://2021.help.altair.com/2021/hwsolvers/acusolve/topics/acusolve/training_manual/renormalization_group_rng_r.htm

Bentley, B. J., & Leal, L. G. (1986). An experimental investigation of drop deformation and breakup in steady, two-dimensional linear flows. *Journal of Fluid Mechanics*, *167*, 241-283. https://doi.org/10.1017/S0022112086002811

Bui, T. D., & Bui, T. R. (1979). Numerical methods for extremely stiff systems of ordinary differential equations. *Applied Mathematical Modelling*, *3*(5), 355-358. https://doi.org/10.1016/S0307-904X(79)80042-6

Guido, S., & Villone, M. (1998). Three-dimensional shape of a drop under simple shear flow. *Journal of Rheology*, *42*(2), 395-415. https://doi.org/10.1122/1.550942

Hill, D. P. (1998). *The computer simulation of dispersed two-phase flow* [Doctoral dissertation, Imperial College London (University of London)]. London, United Kingdom. http://hdl.handle.net/10044/1/8733

Håkansson, A. (2015). Droplet breakup in high-pressure homogenizers. In *Engineering Aspects of Food Emulsification and Homogenization* (pp. 125-148). CRC Press. https://doi.org/10.1201/b18436

Håkansson, A. (2017). Scale-down failed – Dissimilarities between high-pressure homogenizers of different scales due to failed mechanistic matching. *Journal of Food Engineering*, *195*, 31-39. https://doi.org/10.1016/j.jfoodeng.2016.09.019

Håkansson, A. (2022). Effect of inlet chamber design and operation conditions on laminar drop deformation in a production-scale high-pressure homogenizer—A hydrodynamic investigation. *Chemical Engineering Research and Design*, *180*, 333-345. https://doi.org/10.1016/j.cherd.2022.02.033

Håkansson, A. (2024). High-pressure homogenizer valve design modifications allowing intensified drop breakup without increasing power consumption. I. Optimization of current design-principle. *Chemical Engineering and Processing - Process Intensification*, *196*, 109659. https://doi.org/10.1016/j.cep.2023.109659

Håkansson, A. (2025). Drop breakup can occur inside the gap of a high-pressure homogenizer – New evidence from experimental breakup visualizations. *Journal of Food Engineering*, *389*, 112391. https://doi.org/10.1016/j.jfoodeng.2024.112391

Håkansson, A., Olad, P., & Innings, F. (2022). Identification and Mapping of Three Distinct Breakup Morphologies in the Turbulent Inertial Regime of Emulsification—Effect of Weber Number and Viscosity Ratio. *Processes*, *10*(11), 2204. https://doi.org/10.3390/pr10112204

Innings, F. (2005). *Drop Break-up in High-Pressure Homogenisers* [Doctoral dissertation, Lund University]. Lund University Publications. https://lup.lub.lu.se/record/545470

Innings, F. (2015). High-pressure homogenizer design. In M. Rayner & P. Dejmek (Eds.), *Engineering Aspects of Emulsification and Homogenization in the Food Industry, CRC Press Inc., Boca Raton, Florida, USA* (1st ed., pp. 149-168). CRC Press. https://doi.org/10.1201/b18436

Innings, F., Fuchs, L., & Trägårdh, C. (2011). Theoretical and experimental analyses of drop deformation and break-up in a scale model of a high-pressure homogenizer. *Journal of Food Engineering*, *103*(1), 21-28. https://doi.org/10.1016/j.jfoodeng.2010.09.016

Innings, F., Hamberg, L., & Trägårdh, C. (2005). Dynamic modelling of the deformation of a drop in a four-roll mill. *Chemical Engineering Science*, *60*(17), 4771-4779. https://doi.org/10.1016/j.ces.2005.03.020

Innings, F., & Trägårdh, C. (2005). Visualization of the Drop Deformation and Break-Up Process in a High Pressure Homogenizer. *Chemical Engineering & Technology*, *28*(8), 882-891. https://doi.org/10.1002/ceat.200500080

Innings, F., & Trägårdh, C. (2007). Analysis of the flow field in a high-pressure homogenizer. *Experimental Thermal and Fluid Science*, *32*(2), 345-354. https://doi.org/10.1016/j.expthermflusci.2007.04.007

Kadian, D., Kumar, A., Badgujar, P. C., & Sehrawat, R. (2021). Effect of homogenization and microfluidization on physicochemical and rheological properties of mayonnaise. *Journal of Food Process Engineering*, *44*(4), e13661. https://doi.org/10.1111/jfpe.13661

Kelemen, K., Gepperth, S., Koch, R., Bauer, H. J., & Schuchmann, H. P. (2015). On the visualization of droplet deformation and breakup during high-pressure homogenization. *Microfluidics and Nanofluidics*, *19*(5), 1139-1158. https://doi.org/10.1007/s10404-015-1631-z

Lalanne, B., Masbernat, O., & Risso, F. (2019). A model for drop and bubble breakup frequency based on turbulence spectra. *AIChE Journal*, *65*(1), 347-359. https://doi.org/10.1002/aic.16374

Lamb, H. (1993). *Hydrodynamics*. Cambridge University Press.

Maffettone, P. L., & Minale, M. (1998). Equation of change for ellipsoidal drops in viscous flow. *Journal of Non-Newtonian Fluid Mechanics*, *78*(2), 227-241. https://doi.org/10.1016/S0377-0257(98)00065-2

Miller, C. A., & Scriven, L. E. (1968). The oscillations of a fluid droplet immersed in another fluid. *Journal of Fluid Mechanics*, *32*(3), 417-435. https://doi.org/10.1017/S0022112068000832

Mutsch, B., Preiss, F. J., Dagenbach, T., Karbstein, H. P., & Kähler, C. J. (2021). Scaling of Droplet Breakup in High-Pressure Homogenizer Orifices. Part II: Visualization of the Turbulent Droplet Breakup. *ChemEngineering*, *5*(2), 31.

Ni, R. (2024). Deformation and Breakup of Bubbles and Drops in Turbulence. *Annual Review of Fluid Mechanics*, *56*(Volume 56, 2024), 319-347. https://doi.org/10.1146/annurev-fluid-121021-034541

Olad, P., Crialesi Esposito, M., Brandt, L., Innings, F., & Håkansson, A. (2022a). Towards best practice recommendations for turbulence modelling of high-pressure homogenizer outlet chambers – Numerical validation using DNS data. *Chemical Engineering Science*, *258*, 117748. https://doi.org/10.1016/j.ces.2022.117748

Olad, P., Crialesi Esposito, M., Brandt, L., Innings, F., & Håkansson, A. (2022b). A Direct Numerical Simulation Investigation of the One-Phase Flow in a Simplified Emulsification Device. *Journal of Fluids Engineering*, *144*(8). https://doi.org/10.1115/1.4053896

Omidvar, A., & Khaleghi, H. (2012). An Analytical Approach for Calculation of Critical Weber Number of Droplet Breakup in Turbulent Gaseous Flows. *Arabian Journal for Science and Engineering*, *37*(8), 2311-2321. https://doi.org/10.1007/s13369-012-0319-x

Qi, Y., Tan, S., Corbitt, N., Urbanik, C., Salibindla, A. K. R., & Ni, R. (2022). Fragmentation in turbulence by small eddies. *Nature Communications*, *13*(1), 469. https://doi.org/10.1038/s41467-022-28092-3

Rayleigh, L. (1879). On the Capillary Phenomena of Jets. *Proceedings of the Royal Society of London*, *29*, 71-97.

Risso, F., & Fabre, J. (1998). Oscillations and breakup of a bubble immersed in a turbulent field. *Journal of Fluid Mechanics*, *372*, 323-355. https://doi.org/10.1017/S0022112098002705

Roa, I., Renoult, M.-C., Dumouchel, C., & Brändle de Motta, J. C. (2023). Droplet oscillations in a turbulent flow [Original Research]. *Frontiers in Physics*, *Volume 11 - 2023*. https://doi.org/10.3389/fphy.2023.1173521

Roobab, U., Inam-Ur-Raheem, M., Khan, A. W., Arshad, R. N., Zeng, X.-a., & Aadil, R. M. (2023). Innovations in High-pressure Technologies for the Development of Clean Label Dairy Products: A Review. *Food Reviews International*, *39*(2), 970-991. https://doi.org/10.1080/87559129.2021.1928690

Schultz, S., Wagner, G., Urban, K., & Ulrich, J. (2004). High-Pressure Homogenization as a Process for Emulsion Formation. *Chemical Engineering & Technology*, *27*(4), 361-368. https://doi.org/10.1002/ceat.200406111

Siqveland, L. M., & Skjæveland, S. M. (2021). Derivations of the Young-Laplace equation. *Capillarity*, *4*(2), 23-30. https://doi.org/10.46690/capi.2021.02.01

Stang, M., Schuchmann, H., & Schubert, H. (2001). Emulsification in High-Pressure Homogenizers. *Engineering in Life Sciences*, *1*(4), 151-157. https://doi.org/10.1002/1618-2863(200110)1:4<151::AID-ELSC151>3.0.CO;2-D

Stone, H. A. (1994). Dynamics of Drop Deformation and Breakup in Viscous Fluids. *Annual Review of Fluid Mechanics*, *26*(Volume 26, 1994), 65-102. https://doi.org/10.1146/annurev.fl.26.010194.000433

Taglienti, D., Guglietta, F., & Sbragaglia, M. (2023). Reduced model for droplet dynamics in shear flows at finite capillary numbers. *Physical Review Fluids*, *8*(1), 013603. https://doi.org/10.1103/PhysRevFluids.8.013603

Talimi, V., Muzychka, Y. S., & Kocabiyik, S. (2012). A review on numerical studies of slug flow hydrodynamics and heat transfer in microtubes and microchannels. *International Journal of Multiphase Flow*, *39*, 88-104. https://doi.org/10.1016/j.ijmultiphaseflow.2011.10.005

Taylor, G. I. (1932). The viscosity of a fluid containing small drops of another fluid. *Proceedings of the Royal Society of London. Series A, Containing papers of a mathematical and physical character*, *138*(834), 41-48. https://doi.org/10.1098/rspa.1932.0169

Taylor, G. I. (1934). The formation of emulsions in definable fields of flow. *Proceedings of the Royal Society of London. Series A, Containing Papers of a Mathematical and Physical Character*, *146*(858), 501-523. https://doi.org/10.1098/rspa.1934.0169

Walstra, P. (1999). *Dairy Technology: Principles of Milk Properties and Processes*. CRC Press.

Walstra, P., & Smulders, P. E. A. (1998). Emulsion Formation. In B. P. Binks (Ed.), *Modern Aspects of Emulsion Science* (pp. 0). The Royal Society of Chemistry. https://doi.org/10.1039/9781847551474-00056

Windhab, E. J., Dressler, M., Feigl, K., Fischer, P., & Megias-Alguacil, D. (2005). Emulsion processing—from single-drop deformation to design of complex processes and products. *Chemical Engineering Science*, *60*(8), 2101-2113. https://doi.org/10.1016/j.ces.2004.12.003

7 Appendix A

7.1 Simple shear flow

For simple shear flow ($\alpha = 0$), $\widehat{\boldsymbol{W}}$ and $\widehat{\boldsymbol{E}}$ were defined from Eq. 17 and 18, with $\boldsymbol{V}$:

$$\boldsymbol{V} = \begin{bmatrix} 0 & \dot{\gamma} & 0 \\ 0 & 0 & 0 \\ 0 & 0 & 0 \end{bmatrix};\ \widehat{\boldsymbol{W}} = \frac{1}{2}\begin{bmatrix} 0 & 1 & 0 \\ -1 & 0 & 0 \\ 0 & 0 & 0 \end{bmatrix};\ \widehat{\boldsymbol{E}} = \frac{1}{2}\begin{bmatrix} 0 & 1 & 0 \\ 1 & 0 & 0 \\ 0 & 0 & 0 \end{bmatrix} \tag{A1}$$

Inserting $\widehat{\boldsymbol{W}}$ and $\widehat{\boldsymbol{E}}$ in Eq. A1 into Eq. 16 gives L and B as:

$$L^2 = \frac{{f_1}^2 + Ca^2 + f_2 \cdot Ca \cdot \sqrt{{f_1}^2 + Ca^2}}{\left({f_1}^2 + Ca^2\right)^{1/3}\left({f_1}^2 + Ca^2 - {f_2}^2 \cdot Ca^2\right)^{2/3}}, \tag{A2}$$

$$B^2 = \frac{{f_1}^2 + Ca^2 - f_2 \cdot Ca \cdot \sqrt{{f_1}^2 + Ca^2}}{\left({f_1}^2 + Ca^2\right)^{1/3}\left({f_1}^2 + Ca^2 - {f_2}^2 \cdot Ca^2\right)^{2/3}}. \tag{A3}$$

7.2 Pure shear flow

For pure shear flow ($\alpha = 1$), $\boldsymbol{V}$, $\widehat{\boldsymbol{W}}$ and $\widehat{\boldsymbol{E}}$ is defined as:

$$\boldsymbol{V} = \begin{bmatrix} \dot{\varepsilon} & 0 & 0 \\ 0 & -\dot{\varepsilon} & 0 \\ 0 & 0 & 0 \end{bmatrix};\ \widehat{\boldsymbol{W}} = 0;\ \widehat{\boldsymbol{E}} = \begin{bmatrix} 1 & 0 & 0 \\ 0 & -1 & 0 \\ 0 & 0 & 0 \end{bmatrix}, \tag{A4}$$

and L and B are given by:

$$L^2 = \frac{f_1 \cdot g(\widehat{\boldsymbol{S}})}{f1 - 2Ca \cdot f_2}, \tag{A5}$$

$$B^2 = \frac{f_1 \cdot g(\widehat{\boldsymbol{S}})}{f_1 + 2Ca \cdot f_2}, \tag{A6}$$

where:

$$g(\widehat{\boldsymbol{S}}) = \left(\frac{{f_1}^2 + 4Ca^2 \cdot {f_1}^2}{{f_1}^2}\right)^{1/3}. \tag{A7}$$

7.3 General form

The general $\boldsymbol{V}$ with varying α is defined here as (Maffettone & Minale, 1998):

$$\boldsymbol{V} = \begin{bmatrix} 1+\alpha & 1-\alpha & 0 \\ -1+\alpha & -1-\alpha & 0 \\ 0 & 0 & 0 \end{bmatrix}, \tag{A8}$$

which, from Eq. 17 and 18, yields:

$$\widehat{\boldsymbol{W}} = \frac{1}{2}\begin{bmatrix} 0 & 1-\alpha & 0 \\ -1+\alpha & 0 & 0 \\ 0 & 0 & 0 \end{bmatrix};\ \widehat{\boldsymbol{E}} = \frac{1}{2}\begin{bmatrix} 1+\alpha & 0 & 0 \\ 0 & -1-\alpha & 0 \\ 0 & 0 & 0 \end{bmatrix}, \tag{A9}$$

and, from Eq. 16, gives L and B as:

$$L^2 = \left(\frac{\hat{S}_{11}+\hat{S}_{22}}{2}\right) + \sqrt{\left(\frac{\hat{S}_{11}+\hat{S}_{22}}{2}\right)^2 - \hat{S}_{11}\cdot\hat{S}_{22} + \hat{S}_{12}{}^2}, \tag{A10}$$

$$B^2 = \left(\frac{\hat{S}_{11}+\hat{S}_{22}}{2}\right) - \sqrt{\left(\frac{\hat{S}_{11}+\hat{S}_{22}}{2}\right)^2 - \hat{S}_{11}\cdot\hat{S}_{22} + \hat{S}_{12}{}^2}. \tag{A11}$$

Here, $\hat{S}_x$ denotes the matrix positions in $\widehat{\boldsymbol{S}}$:

$$\widehat{\boldsymbol{S}} = \begin{bmatrix} \hat{S}_{11} & \hat{S}_{12} & \hat{S}_{13} \\ \hat{S}_{21} & \hat{S}_{22} & \hat{S}_{23} \\ \hat{S}_{31} & \hat{S}_{32} & \hat{S}_{33} \end{bmatrix}, \tag{A12}$$

$$\hat{S}_{11} = \frac{\hat{S}_{12}\cdot Ca\cdot(1-\alpha) + f_1\cdot g\left(\widehat{\boldsymbol{S}}\right)}{f_1 - Ca\cdot f_2\cdot(1+\alpha)}, \tag{A13}$$

$$\hat{S}_{22} = \frac{\hat{S}_{12}\cdot Ca\cdot(\alpha-1) + f_1\cdot g\left(\widehat{\boldsymbol{S}}\right)}{f_1 + Ca\cdot f_2\cdot(1+\alpha)}, \tag{A14}$$

$$\hat{S}_{12} = \frac{Ca\cdot(1-\alpha)\cdot\left(\hat{S}_{22}-\hat{S}_{11}\right)}{2f_1}. \tag{A15}$$

From the boundary condition of constant drop volume, $III_S = 1$, Eq. 20 and 21 results in:

$$g\left(\widehat{\boldsymbol{S}}\right) = \frac{3}{\hat{S}_{11}\cdot\hat{S}_{22} - \left(\hat{S}_{12}\right)^2}. \tag{A16}$$

7.4 Numerical and empirical validation

For the Maffettone-Minale model, the analytical solution was validated numerically by solving a system of equations. The simple shear flow was solved by inserting Eq. A1 into Eq. 16 which resulted in the same equations for the general form (Eq. 29 and 30):

$$L^2 = \left(\frac{\hat{S}_{11} + \hat{S}_{22}}{2}\right) + \sqrt{\left(\frac{\hat{S}_{11} + \hat{S}_{22}}{2}\right)^2 - \hat{S}_{11} \cdot \hat{S}_{22} + \hat{S}_{12}{}^2}, \quad (A17)$$

$$B^2 = \left(\frac{\hat{S}_{11} + \hat{S}_{22}}{2}\right) - \sqrt{\left(\frac{\hat{S}_{11} + \hat{S}_{22}}{2}\right)^2 - \hat{S}_{11} \cdot \hat{S}_{22} + \hat{S}_{12}{}^2}, \quad (A18)$$

where $\hat{S}_x$ denotes the matrix positions in $\widehat{\boldsymbol{S}}$:

$$\widehat{\boldsymbol{S}} = \begin{bmatrix} \hat{S}_{11} & \hat{S}_{12} & \hat{S}_{13} \\ \hat{S}_{21} & \hat{S}_{22} & \hat{S}_{23} \\ \hat{S}_{31} & \hat{S}_{32} & \hat{S}_{33} \end{bmatrix}, \quad (A19)$$

$$\hat{S}_{11} = \frac{\hat{S}_{12} \cdot Ca \cdot (f_2 + 1)}{f1} + g(\widehat{\boldsymbol{S}}), \quad (A20)$$

$$\hat{S}_{22} = \frac{\hat{S}_{12} \cdot Ca \cdot (f_2 - 1)}{f1} + g(\widehat{\boldsymbol{S}}), \quad (A21)$$

$$\hat{S}_{12} = \frac{\hat{S}_{11} \cdot Ca \cdot (f_2 - 1)}{2f_1} + \frac{\hat{S}_{22} \cdot Ca \cdot (f_2 + 1)}{2f_1}. \quad (A22)$$

From the boundary condition of constant drop volume, $III_S = 1$, Eq. 20 and 21 results in:

$$g(\widehat{\boldsymbol{S}}) = \frac{3}{\hat{S}_{11} \cdot \hat{S}_{22} + \hat{S}_{11} \cdot g(\widehat{\boldsymbol{S}}) + \hat{S}_{22} \cdot g(\widehat{\boldsymbol{S}}) - (\hat{S}_{12})^2}, \quad (A23)$$

$\hat{S}_{12}$ and $g(\widehat{\boldsymbol{S}})$ were solved by rearranging Eq. A22 and A23 to equal zero and using the scipy.optimize.root function with the "hybr" method. This let $\hat{S}_{11}$, $\hat{S}_{12}$, $\hat{S}_{22}$ and $g(\widehat{\boldsymbol{S}})$ to be known which solved, Eq. A1 and A18. (A) and (D) in Figure A1 shows similar results as Maffettone & Minale (1998) with $D_0 = 0.10$ mm.

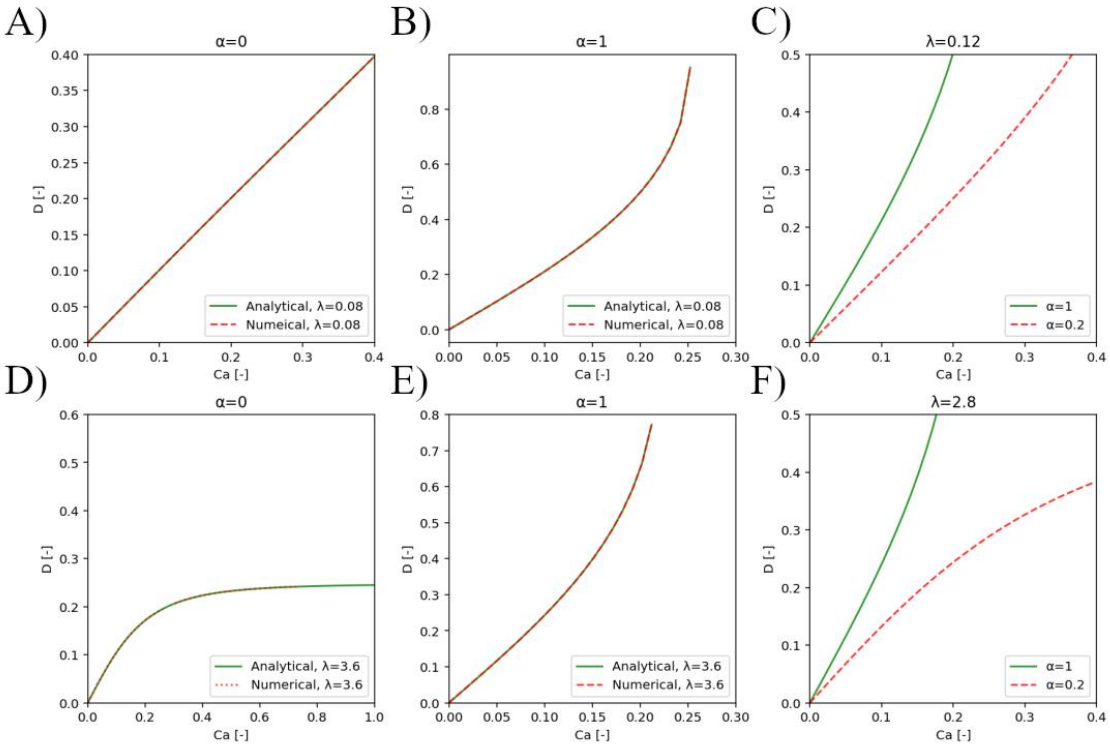

Figure A1: validation of the Maffettone-Minale model with $D_0 = 0.10$ mm. (A) and (D) show simple shear flow for the analytical solution (from Eq. 24 and 25) and numerical (Eq. A1 and A18) for $\lambda = 0.08$ and 3.6, respectively. (B) and (E) show the analytical (Eq. 26 and 27) and numerical (Eq. A24 and A25) solution for the pure shear flow with the same λ as (A) and (D). (C) and (F) shows only the numerical solution for the complex flow (Eq. 29 and 30) with $\alpha = 1$ and 0.2 with $\lambda = 0.12$ and $\lambda = 2.8$, respectively.

The solution for the pure shear flow is validated in a similar way by inserting Eq. A4 into Eq. 16 which directly gives the eigenvalues to be $\hat{S}_{11}$ and $\hat{S}_{22}$:

$$L^2 = \frac{f_1 \cdot g(\hat{\boldsymbol{S}})}{f1 - 2Ca \cdot f_2}, \tag{A24}$$

$$B^2 = \frac{f_1 \cdot g(\hat{\boldsymbol{S}})}{f_1 + 2Ca \cdot f_2}. \tag{A25}$$

With the same boundary condition of $III_S = 1$, Eq. 20 and 21 gives:

$$g(\hat{\boldsymbol{S}}) = \left(\frac{{f_1}^2 + 4Ca^2 \cdot {f_2}^2}{{f_1}^2}\right)^{1/3}, \tag{A26}$$

with the solution for the deformation D shown in Figure A1 (B) and (D). For validation of the general flow, Eq. 29 and 30 were solved and the D for different Ca are shown Figure A1 (C) and (F) for different λ and α.

8 Appendix B

8.1.1.1 The Lamb method

The Lamb method defines β_2 and ω_2 as (Lamb, 1993):

$$\beta_2 = \frac{4(15\mu_D + 40\mu_C)}{(3\rho_D + 2\rho_C) \cdot {D_0}^2}, \tag{B1}$$

$$\omega_2 = \frac{192\sigma}{(3\rho_D + 2\rho_C) \cdot {D_0}^3}. \tag{B2}$$

8.1.1.2 The Miller-Scriven method

For the Miller-Scriven method, β_n and ω_n are the real and imaginary part, respectively, of the time factor T_n (Miller & Scriven, 1968):

$$T_n = \beta_n + i \cdot \omega_n. \tag{B3}$$

A positive and negative β_n represent decay and amplification, respectively. Here it is assumed to only be decay, thus a damping rate so that β_n is negative. β_n and ω_n are here defined as:

$$\beta_n = B_1(n) + B_2(n), \tag{B4}$$

$$\omega_n = {\omega_2}^0 - \frac{(2n+1)^2\sqrt{{\omega_2}^0 \cdot \mu_D \cdot \mu_C \cdot \rho_D \cdot \rho_C}}{2\sqrt{2} \cdot D_0 \cdot \left(\rho_C \cdot n + \rho_D \cdot (n+1)\right) \cdot \left(\sqrt{\mu_D \cdot \rho_D} + \sqrt{\mu_C \cdot \rho_C}\right)}, \tag{B5}$$

$$B_1(n) = \frac{(2n+1)^2 \cdot \sqrt{{\omega_2}^0 \cdot \mu_D \cdot \mu_C \cdot \rho_D \cdot \rho_C}}{2\sqrt{2} \cdot D_0 \cdot \left(\rho_C \cdot n + \rho_D \cdot (n+1)\right) \cdot \left(\sqrt{\mu_D \cdot \rho_D} + \sqrt{\mu_C \cdot \rho_C}\right)}, \tag{B6}$$

$$B_2(n) = \frac{(2n+1) \cdot 2(l^2-1) \cdot Z(n)}{2{D_0}^2 \cdot \left(\rho_C \cdot n + \rho_D \cdot (n+1)\right) \cdot \left(\sqrt{\mu_D \cdot \rho_D} + \sqrt{\mu_C \cdot \rho_C}\right)}, \tag{B7}$$

$$Z(n) = {\mu_D}^2 \cdot \rho_D + 2n \cdot (n+2) \cdot {\mu_C}^2 \cdot \rho_C + \mu_D \cdot \mu_C \cdot (\rho_D \cdot (n+2) - \rho_C \cdot (n-1)), \tag{B8}$$

where ${\omega_2}^0$ is the inviscid oscillation frequency:

$${\omega_2}^0 = \sqrt{\frac{\sigma \cdot n \cdot (n+1)(n-1)(n+2)}{{D_0}^3 \cdot \left(\rho_C \cdot n + \rho_D \cdot (n+1)\right)}}. \tag{B9}$$

8.1.1.3 The Lalanne method

The Lalanne method set Eq. B2 to be the inviscid frequency ${\omega_2}^0$ and defines β_2 and ω_2 as (Lalanne et al., 2019):

$$\beta_2 = \frac{{\omega_2}^0}{Re_{OSC}} \cdot \left(F_L \cdot \sqrt{Re_{OSC}} - 2{F_L}^2 + G_L\right), \tag{B10}$$

$$\omega_2 = {\omega_2}^0 \cdot \left(1 - \frac{F_L}{\sqrt{Re_{OSC}}}\right), \tag{B11}$$

$${\omega_2}^0 = \frac{192\sigma}{(3\rho_D + 2\rho_C) \cdot {D_0}^3}, \tag{B12}$$

$$Re_{OSC} = \frac{\rho_D \cdot {\omega_2}^0 \cdot {D_0}^2}{4\mu_D}, \tag{B13}$$

$$G_L = \frac{5(6 + 5\hat{\mu} - \hat{\rho} \cdot \hat{\mu} + 16\hat{\rho} \cdot \hat{\mu}^2)}{(4\hat{\rho} - 6) \cdot \left(1 + \sqrt{\hat{\rho} \cdot \hat{\mu}}\right)^2}, \tag{B14}$$

$$F_L = \frac{25\sqrt{\hat{\rho} \cdot \hat{\mu}}}{2\sqrt{2}(\hat{\rho} + 3) \cdot \left(1 + \sqrt{\hat{\rho} \cdot \hat{\mu}}\right)}, \tag{B15}$$

where $\hat{\rho} = (\rho_C/\rho_D)$ and $\hat{\mu} = (\mu_C/\mu_D)$.

8.1.1.4 The Roa method

(Roa et al., 2023) studied drop oscillation in a turbulent flow regime and define β_n and ω_n as:

$$\beta_n = {\omega_n}^0 \cdot \left(A_R - 2{A_R}^2\right) + \frac{B_R}{2(n \cdot \hat{\rho} + n + 1) \cdot \left(1 + \sqrt{\hat{\rho} \cdot \hat{\mu}}\right)^2} \cdot \frac{4\mu_D}{{D_0}^2 \cdot \rho_D}, \quad (C16)$$

$$\omega_n = {\omega_n}^0 \cdot \left(1 - \frac{(2n+1)^2 \cdot \sqrt{\hat{\rho} \cdot \hat{\mu}}}{A_R}\right), \quad (C17)$$

$$A_R = 2\sqrt{{\omega_n}^0 \cdot \frac{\rho_D}{\mu_D}} \cdot D_0 \cdot \left(n \cdot \hat{\rho} + (n+1)\right) \cdot \left(1 + \sqrt{\hat{\rho} \cdot \hat{\mu}}\right), \quad (C18)$$

$$B_R = (2+n) \cdot (2(n^2-1) + (n+2) \cdot \hat{\mu} - (n-1) \cdot \hat{\rho} \cdot \hat{\mu} + 2n \cdot (n+2) \cdot \hat{\rho} \cdot \hat{\mu}^2), \quad (C19)$$

with the inviscid frequency and damping rate ${\omega_2}^0$ and ${\beta_2}^0$, respectively:

$${\omega_n}^0 = \sqrt{\frac{8n \cdot (n+1) \cdot (n-1) \cdot (n+2) \cdot \sigma}{{D_0}^3 \cdot (n \cdot \rho_C + (n+1) \cdot \rho_D)}}, \quad (C20)$$

$${\beta_n}^0 = (2n+1) \cdot (n-1) \cdot \frac{4\mu_D}{\rho_D \cdot {D_0}^2}. \quad (C21)$$

9 Appendix C

9.1.1 Mesh independence study: Steady state CFD

Mesh dependence of the droplet deformation L/B, calculated with the Weber model, was examined for three particle trajectories over different mesh resolutions. The Weber model was applied to particle trajectory ID 0, 1 and 2 (See Figure C1 for trajectories).

In total, six meshes were compared, numbered from zero to five. Each refinement applied to a control area splits it into four new cells, thus halving the lattice length of the cell. The first refinement was conducted by applying one near wall cell-register, corresponding to a 0.2 mm distance from the walls followed by one refinement of the entire geometry. Subsequentially all refined meshes possess two average cell sizes, with the cells within 0.2 mm from the walls being of half the lattice length of the cells in the bulk.

Table C1: Mesh densities examined during steady state CFD mesh independence study. Including the mesh index, average lattice length in bulk, the total number of cells and the cells traversed by each trajectory.

Refinement index	Average lattice length in bulk [μm]	Number of cells in mesh, total.	Number of cells traversed by particle trajectory:		
			0	1	2
0	200	534	206	197	176
1	100	3 448	258	252	246
2	50	11 055	246	367	357
3	25	36 514	399	503	550
4	12.5	84 030	690	860	968
5	6.25	298 435	1 066	1 307	1 582

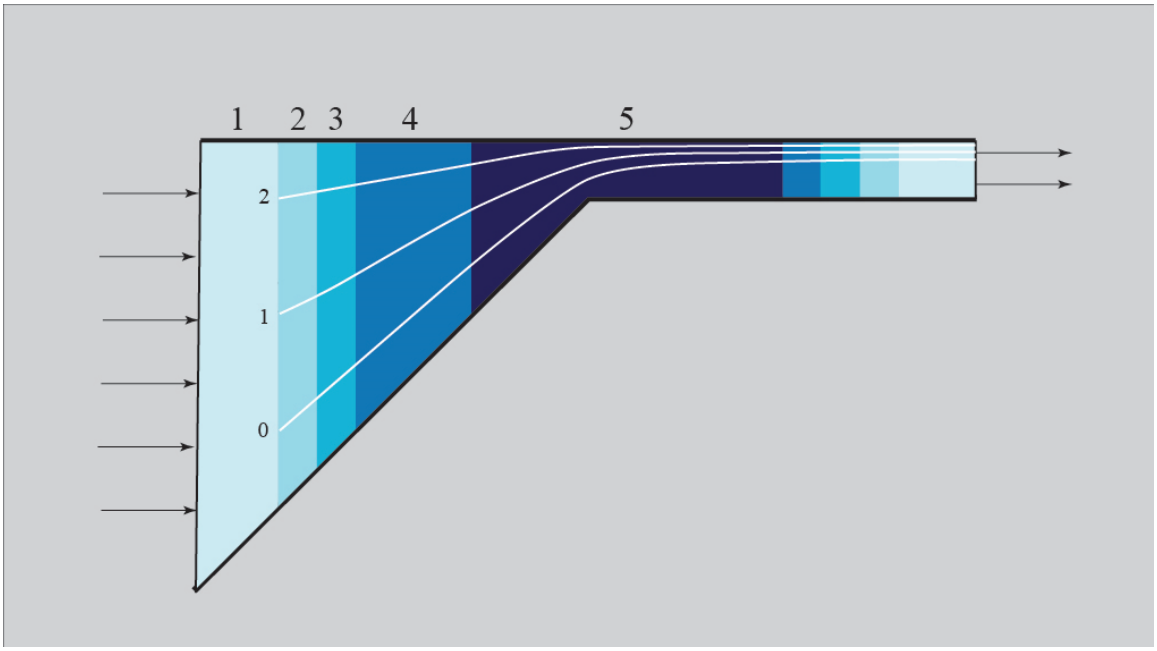

Figure C1: Illustration of the different cell registers applied during mesh refinement. The registers are continuous but overlayed so that register 1 thus span the entire geometry, while register 2 is slightly contracted from both the inlet and outlet. The cell registers are subsequently further incrementally contracted from the inlet and outlet. The white lines illustrate the three particle trajectories.

The average lattice length, total number of cells of each mesh and the number of cells traversed by each of the three simulated particle tracts are displayed in Table C1. Note that trajectories one and two interact more with the extra dense near-wall refinement region, explaining the larger number of cells traversed by these compared to trajectory zero. Figure C1 displays the different cell registers applied for each successive refinement, excluding the near-wall register.

The relative difference between the calculated deformation, L/B, for each mesh refinement compared to the most refined mesh was calculated as follows

$$\text{Relative difference of } N_i = \left(\frac{N_i - N_{final}}{N_{final}}\right) \cdot 100\%, \tag{C1}$$

where N_i is the calculated deformation for one trajectory in one mesh resolution and N_{final} is the corresponding deformation in the most resolved mesh simulation. These differences are plotted in Figure C2 for all three trajectories. The droplet deformation quickly converged using the Weber model, with even the maximal divergence from the most refined series being below 1% in all cases.

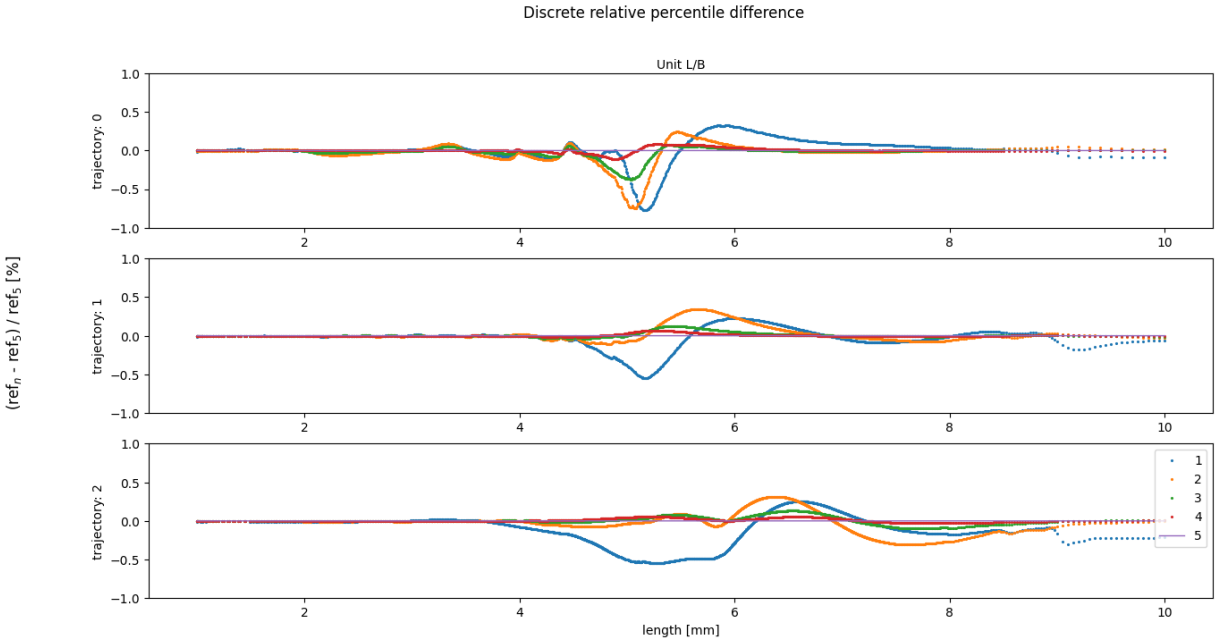

Figure C2: The percentile relative difference between the drop deformation L/B, calculated as the difference at the corresponding position in the most refined simulation divided by the corresponding value at the most refined simulation. L and B were calculated using the Weber model.

9.1.2 Mesh independence study: Transient CFD

During the mesh independence study for the transient two-phase simulations, the same mesh geometry was used as in the steady state simulations. However, only the meshes corresponding to refinements 2, 3, 4 and 5 in Table C1 were used. Timestep lengths were chosen for each mesh density to limit the maximal Courant number, Co, to below one. The significance of Co is explained in section 3.3. The maximal Co occur by the pivot point where the sloped wall meets the gap entrance, the simulated oil droplets do not, however, pass through this area. The Co of the cells interacted with by the droplet are therefore far lower than one.

The variable examined during the mesh dependence study was the droplet deformation, L/B. The deformation was calculated by exporting contour plots of the phase system continuously during simulation which were subsequently processed with the same algorithm used for the experimental valve setup. The simulation however did not converge in the mesh densities examined instead diverging, as seen Figure C3 below.

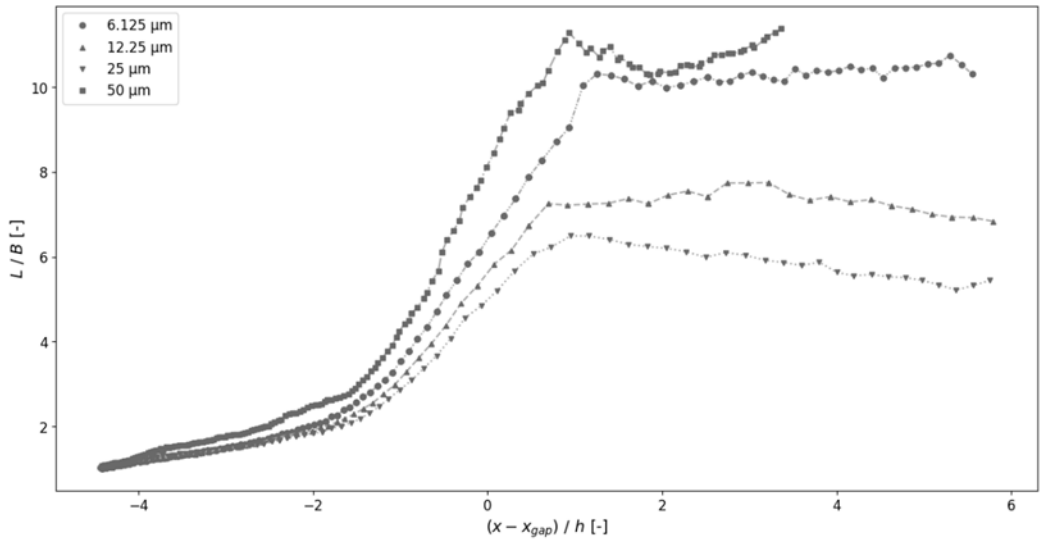

Figure C3: Simulated droplet deformation of an oil drop, 0.5 mm in diameter, traversing the flow geometry over different mesh densities. The average lattice lengths shown are 50 (▼), 25 (▲), 12.5 (●) and 6.25 (■) µm*. The x-axis describes the horizontal length traversed by the drop in gap lengths, where x = 0 is the horizontal position of the gap inlet.*

9.1.3 Laplace pressure implications for interfacial tension modelling

The simulated oil droplets show greater and more persistent elongation compared to the experimentally observed droplet behaviour. A possible factor to this discrepancy is the 2D-modelling. The 2D system does not model a droplet but a cross-section of a cylinder of infinite out-of-plane length, which has implications on the deformation behaviour. The Laplace pressure $\Delta P_{LaPlace}$ (N·m^{-2}), also present in Eq. 1, is dependent on the principal radii of curvature which is also the pressure difference over the phase boundary. It can be calculated as follows,

$$\Delta P_{LaPlace} = \gamma \cdot \left(\frac{1}{r_1} + \frac{1}{r_2}\right). \qquad (C2)$$

The principal radii of curvature, r_1 and r_2, represent the largest and smallest degrees of curvature at a point on the surface of an object, as curvature decreases the radius of curvature increases. The difference in Laplace pressure for a perfect sphere and a cylinder of the same diameter can thus be described. In a sphere the radii of curvature are equal yielding

$$\Delta P_{LaPlace,\ sphere} = \gamma \cdot \frac{2}{r_1}. \qquad (C3)$$

In a cylinder one axis is straight and not curved, the radius of curvature will thus approach infinity yielding

$$\Delta P_{LaPlace,\ cylinder} = \gamma \cdot \left(\frac{1}{r_1} + 0\right) = \gamma \cdot \frac{1}{r_1}. \qquad (C4)$$

The Laplace pressure differs between a sphere and a cylinder, of equal radius, by factor two.

The difference, in Laplace pressure, between the 2D simulated droplet and the real 3D droplet can only be described as the difference between a cylinder and a sphere when the droplet is not deformed. As the droplet elongates points along the broadsides of the ellipse will lose their 2D curvature as well thus approaching $\Delta P_{LaPlace} = 0$, whilst the 3D equivalent keeps the large out-of-plane curvature around the minor elliptical axis. Therefore, the discrepancy between the 2D- and 3D Laplace pressures increases with elongation.

To account for the 2D-model assuming the cross-section of a cylinder another convergence study was carried out with an effective interfacial tension coefficient $\gamma_{eff} = 2 \cdot \gamma$, 26 mN·m^{-1}. To better approximate sphericity in the Laplace pressure calculation to investigate if a simple increase in γ would yield better simulations.

The graphical determination of the deformation, L/B, was also considered a possible source of error, as the actual phase boundary is sharp but is expressed as a gradient in the software. The size of the boundary gradient depends on mesh resolution, decreasing with finer mesh sizes. The uncertainty in graphically determining the boundary layer for the minor axis is compounded by the great degree of elongation making the minor axis smaller and the boundary region proportionally larger. The major axis is however less sensitive to this error since it is proportionally much longer than the boundary gradient. In order to mitigate this uncertainty, the deformation was calculated using the numerically calculated phase area, retrieved from the simulation software, in combination with the graphically determined major axis. Eliminating the need for graphically determining the minor axis:

$$A_{ellipse} = \pi \cdot L \cdot B \ \Leftrightarrow \ \frac{L}{B} = \frac{\pi \cdot L^2}{A_{ellipse}}\ . \qquad (C5)$$

A mesh independence study was carried out with an interfacial tension coefficient of 26 mN·m^{-1}, the deformation was calculated graphically and with the hybrid method using the numerically determined oil phase area. The results are shown in Figure C4.

Mesh independence was not achieved and the finest mesh diverged, however, the divergence mainly occurs after the gap position, the simulated deformation is less mesh-dependent before the gap. The maximal deformation simulated (~5.0) is lower than the 13 mN· m^{-1}, simulation (~11) but still significantly larger than the empirical data (~2.5).

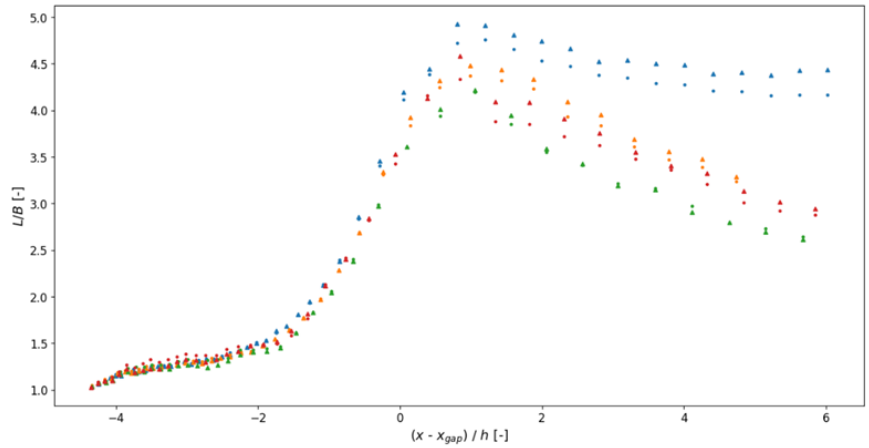

Figure C4: Simulated droplet deformation of a 0.5 mm diameter droplet with an interfacial tension coefficient of 26 mN·m^{-1}, traversing the flow geometry over different mesh densities. The average bulk lattice length shown are 50 (red), 25 (green), 12.5 (orange) and 6.25 (blue) (µm). The deformation was calculated with graphically determined major and minor axes (●) graphically determined major axis and numerically calculated phase area (▲). The x-axis describes the horizontal length traversed by the drop in terms of gap lengths, where x = 0 is the horizontal position of the gap inlet.

To investigate if the observed droplet behaviour could be more accurately modelled with an empirically fitted greater γ_{eff} the same method was applied with $\gamma_{eff} = 8\gamma$. The results of which are presented in Figure C5.

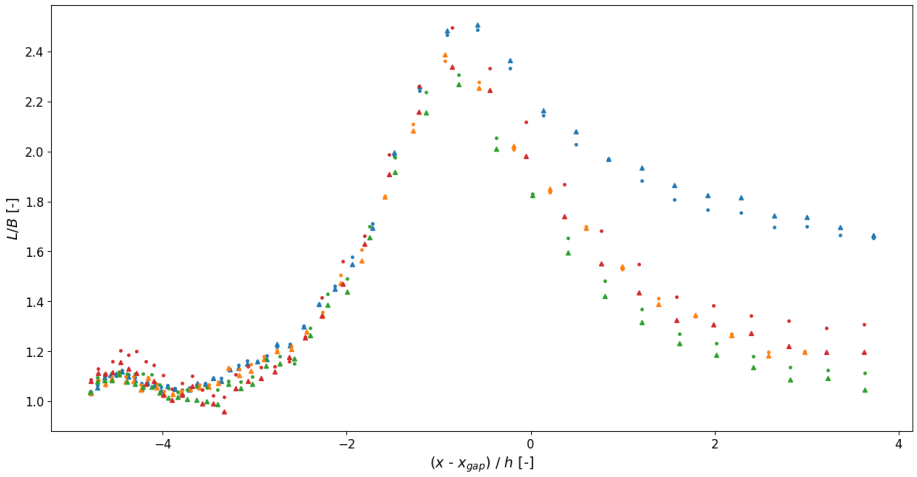

Figure C5: Simulated droplet deformation of a 0.5 mm diameter droplet with an interfacial tension coefficient of 206 mN·m^{-1}, in different mesh densities. The average bulk lattice length shown are 50 (red), 25 (green), 12.5 (orange) and 6.25 (blue) µm. *The deformation was calculated with graphically determined major and minor axes (●) graphically determined major axis and numerically calculated phase area (▲). The x-axis describes the horizontal length traversed by the drop in terms of gap lengths, where x = 0 is the horizontal position of the gap inlet.*

Empirical fitting of γ_{eff} was deemed promising and further studied. The mesh density with lattice length 25 μm, green in Figure C4 and Figure C5, was chosen since it is less computationally demanding and higher mesh densities failed to yield noticeable increases in mesh independence.

10 Appendix D

The flow trajectory and deformation of the experimentally observed oil droplet series for flow rates 1.03, 1.36 and 1.51 L·min^{-1} are depicted in Figures D1 and D2, respectively.

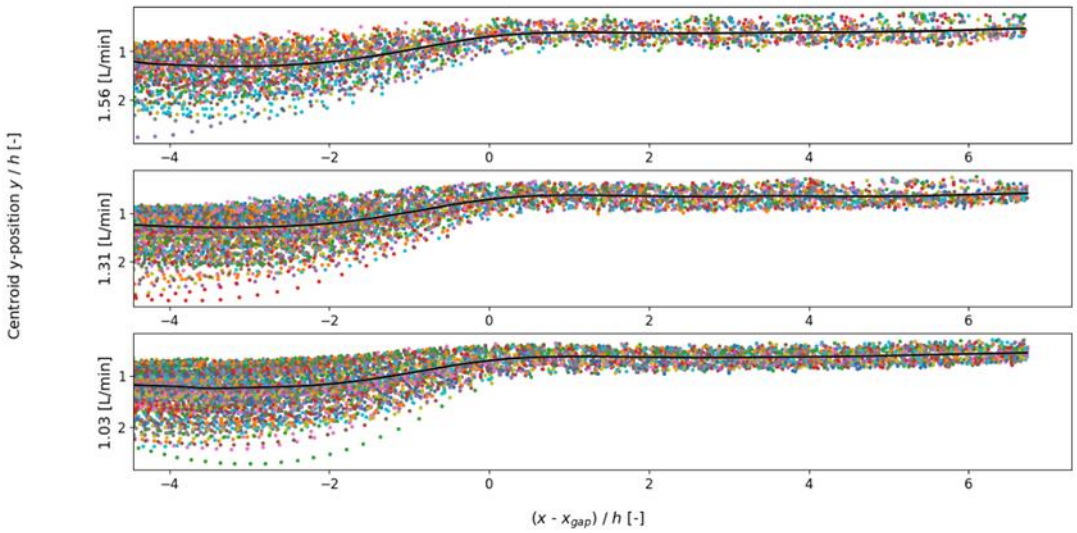

Figure D1: Oil droplet flow trajectory in lengths of gap heights (0.75 mm). The scatterplot represents the droplet centroid position in different series over the flow geometry. The solid black curve is the LOWESS (10%) filtered curve for the scatterplot.

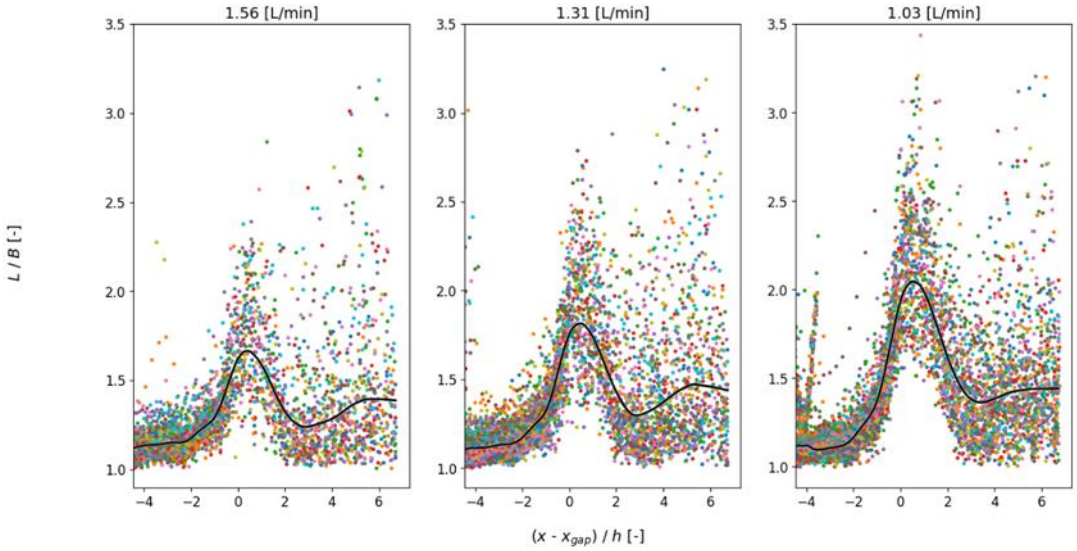

Figure D2: Oil droplet deformation, major elliptical axis divided by minor elliptical axis, by horizontal position given in gap height (0.75 mm). The horizontal position represents the droplet centroid position over the horizontal flow axis. The solid black curve represents the LOWESS (10%) filtered curve of the scatterplot.

11 Appendix E

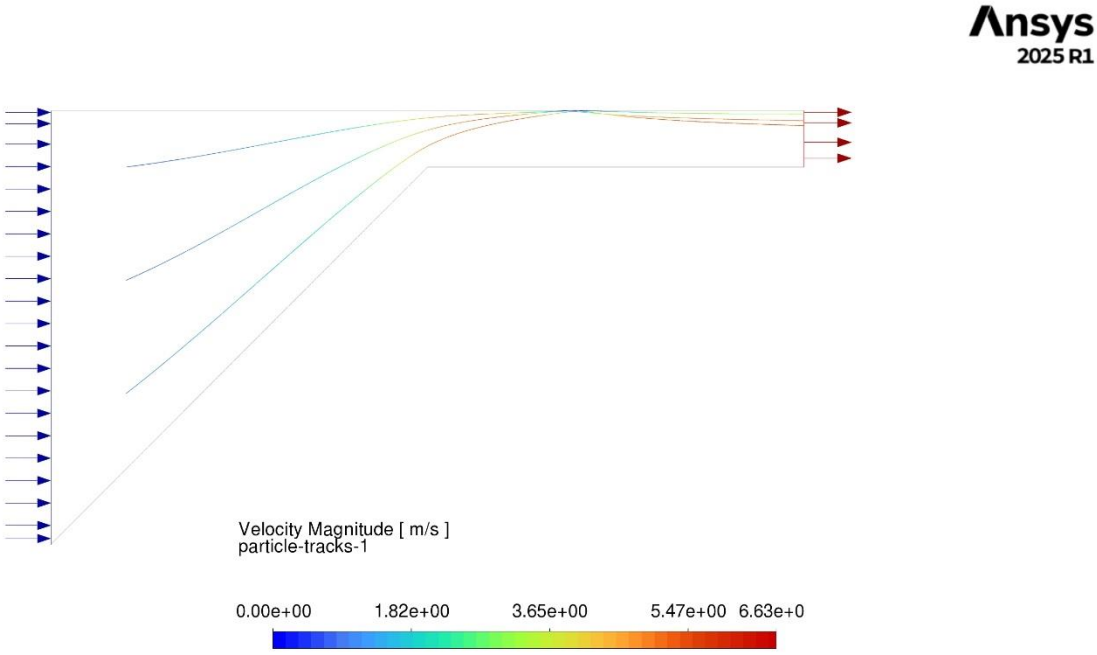

Figure E1: Particle trajectories with $D_0 = 0.35$ mm, $v_{in} = 0.603$ m·s^{-1} ($Q = 1.51$ L·min^{-1}), $\rho_D = 950$ kg·m^{-3}, 1 mm from the inlet and evenly spread between y=2 and y=5. The colour gradient represents the velocity magnitude for the continuous phase.

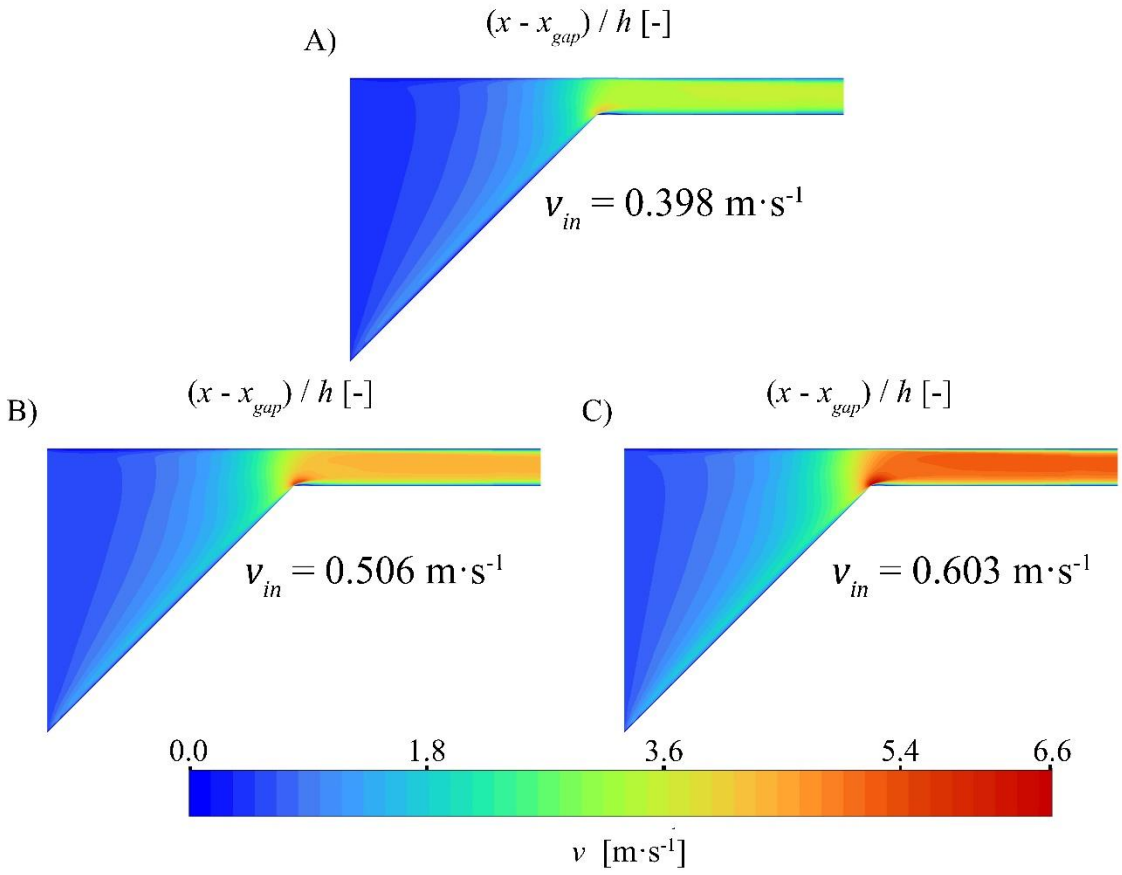

Figure E2: Illustration of the velocity magnitude contour plots for the continuous phase at varying inlet velocities. (A) v_{in} = 0.398 m·s^{-1} (Q = 1.03 L·min^{-1}), (B) v_{in} = 0.506 m·s^{-1} (Q = 1.31 L·min^{-1}) and (C) v_{in} = 0.603 m·s^{-1} (Q = 1.56 L·min^{-1}). The length scale is in gap heights, $(x - x_{gap})/h$, and the colour gradients represent the velocity magnitude v (m·s^{-1}).

12 Appendix F

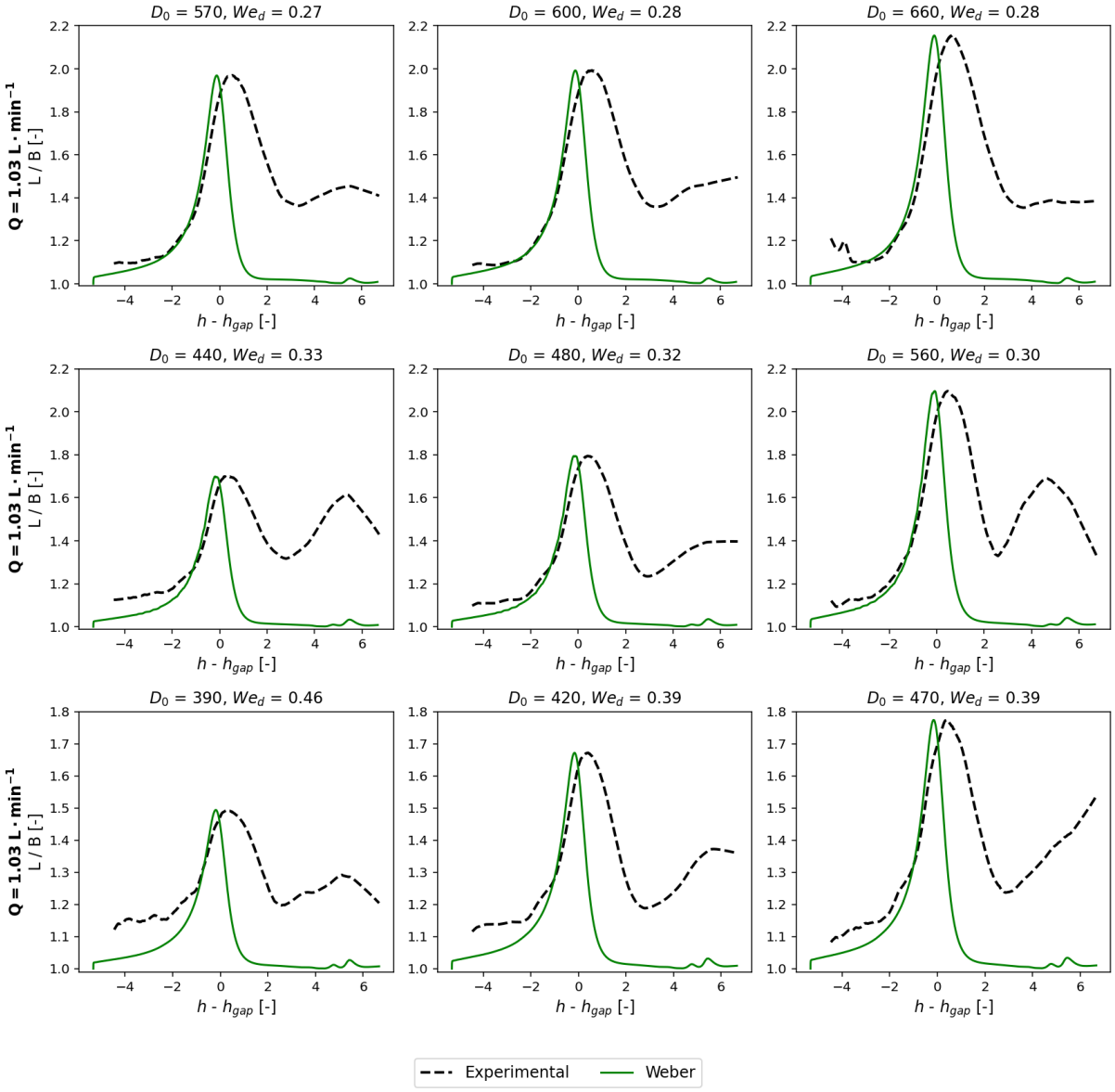

Figure F1: Drop deformation L/B for the Weber model with optimised We_d (green line), and LOWESS-filtered empirical data (black dashed line). The L/B for the Weber model was calculated along the trajectories for particle ID 1 for $Q = 1.03$ (upper row), 1.31 (middle row) and 1.56 (lower row) L·min^{-1}. The values for We_d was optimised for the model to have the same maximum L/B as the empirical data.